TECHNISCHE UNIVERSITÄT WIEN

Bereich Laser und Lasergestützte Fertigung

Diplomarbeit

Sub-Micron Ablation of Chromium based Thin-Films for Optical Data Storage

ausgeführt zum Zwecke der Erlangung des akademischen Grades eines

Diplomingenieurs (Dipl. Ing. oder DI)

eingereicht an der TU Wien, Fakultät für Maschinenwesen und Betriebswissenschaften

von

Lukas KREUZIGER

Matrikelnummer: 01525687

Unter der Leitung von

Univ.Prof. Dipl.-Phys. Dr.-Ing. Andreas Otto
Ao.Univ.Prof. Dipl.-Ing. Dr.techn. Gerhard Liedl
Dipl.-Ing. Gerald Humenberger
Projektass. Dipl.-Ing. Roland Fürbacher

E 311 - Institute of Production Engineering and Photonic Technologies

Unterschrift Lukas Kreuziger

Declaration of Authorship

Affidavit

I declare in lieu of oath, that I wrote this thesis and carried out the associated research myself, using only the literature cited in this volume. If text passages from sources are used literally, they are marked as such.

I confirm that this work is original and has not been submitted for examination elsewhere, nor is it currently under consideration for a thesis elsewhere. I acknowledge that the submitted work will be checked electronically-technically using suitable and state-of-the-art means (plagiarism detection software). On the one hand, this ensures that the submitted work was prepared according to the high-quality standards within the applicable rules to ensure good scientific practice "Code of Conduct" at the TU Wien. On the other hand, a comparison with other student theses avoids violations of my personal copyright.

Eidesstattliche Erklärung

Ich erkläre an Eides statt, dass die vorliegende Arbeit nach den anerkannten Grundsätzen für wissenschaftliche Abhandlungen von mir selbstständig erstellt wurde. Alle verwendeten Hilfsmittel, insbesondere die zugrunde gelegte Literatur, sind in dieser Arbeit genannt und aufgelistet. Die aus den Quellen wörtlich entnommenen Stellen, sind als solche kenntlich gemacht.

Das Thema dieser Arbeit wurde von mir bisher weder im In- noch Ausland einem_r Beurteiler_in zur Begutachtung in irgendeiner Form als Prüfungsarbeit vorgelegt. Diese Arbeit stimmt mit der von den Begutachter_innen beurteilten Arbeit überein.

Ich nehme zur Kenntnis, dass die vorgelegte Arbeit mit geeigneten und dem derzeitigen Stand der Technik entsprechenden Mitteln (Plagiat-Erkennungssoftware) elektronisch-technisch überprüft wird. Dies stellt einerseits sicher, dass bei der Erstellung der vorgelegten Arbeit die hohen Qualitätsvorgaben im Rahmen der geltenden Regeln zur Sicherung guter wissenschaftlicher Praxis „Code of Conduct“ an der TU Wien eingehalten wurden. Zum anderen werden durch einen Abgleich mit anderen studentischen Abschlussarbeiten Verletzungen meines persönlichen Urheberrechts vermieden.

Wien, Dezember 2023

Unterschrift Lukas Kreuziger

Abstract

Abstract

In recent years industry and scientific research tend to show more and more ambitions to employ lasers not only in the well established field of macro-processing, but also in micro- and nano-machining. Areas of application are, among others, cutting, drilling, marking, and also surface engineering.

In this thesis the technically realizable limits of feature sizes with a femtosecond machining setup shall be evaluated through a suitable choice of processing parameters as well as the processed material system. Furthermore, these results shall be utilized in the form of information storage.

During this evaluation the correlation between the achievable feature size as well as the ablation threshold and the used Laser and material parameters like wavelength, number of pulses per spot, thin film material and film thickness shall be investigated.

Kurzfassung

In jüngster Zeit zeigen Industrie und Forschung immer häufiger Ambitionen Laser nicht nur im bereits etablierten Feld der Makrobearbeitung, sondern auch in der Mikro- und Nanobearbeitung einzusetzen. Anwendungsfelder sind in vielen Bereichen wie Schneiden, Bohren, Markieren, aber auch in der Oberflächentechnik zu finden.

In dieser Arbeit soll versucht werden durch geeignete Wahl sowohl der Bearbeitungsparameter, als auch der zu bearbeitenden Materialsysteme die Grenzen der technisch realisierbaren Strukturgrößen einer Femtosekunden-Bearbeitungsanlage zu ermitteln. Darüber hinaus sollen die gewonnenen Erkenntnisse auch teilweise in Form von Informationsspeicherung angewendet werden.

Im Zuge dessen soll untersucht werden, wie sowohl die Ablationsschwelle, als auch die erreichbare Strukturgröße von der Laser-Wellenlänge, der Anzahl der Pulse pro Bearbeitungspunkt, des Materials der zu bearbeitenden dünnen Schicht und der Dicke des Schichtsystems abhängen.

Contents

1 Theory

1.1 Ultrashort Laser Pulses

Looking at the history of pulsed lasers, there is a clear trend towards shorter and shorter pulses, driven by the desire to understand reactions and interactions taking place at very short periods of time. Ultrashort laser pulses are not clearly defined per se, but are usually referred to pulses in the sub-picosecond regime ($1ps \quad \hat{=} \quad 10^{-12}s$). A prominent example of an Ultrashort laser is the Ti:Sa-laser (Titanium:Sapphire), which is capable of emitting pulses below 100 *fs*.

To put these very short time-spans into perspective, the distance x equal to the speed of light in vacuum c times the duration of the ultrashort Laser pulse can be calculated ($x = t * c$). In a vacuum light travels with a velocity of $c = 299792458 \quad \frac{m}{s}$, so in one second light covers approximately $\frac{3}{4}$ of the distance from the earth to the moon. In one picosecond ($10^{-12} \quad [s]$), light travels less than half of a millimeter and in one femtosecond ($10^{-15} \quad [s]$) less than half of a micrometer, or in other words only about $\frac{1}{100}$ of the thickness of a human hair. [4, p. 1 : 9] [9, p. 1 : 4]

1.1.1 Description and Propagation of Laser Pulses

Starting at Maxwells's Equations, which describe the relationships between the electric field $\mathbf{E}$ and the magnetic field $\mathbf{H}$, a wave equation for the propagation of an electromagnetic wave, and therefore laser-light, can be found:

$$\nabla^2 \mathbf{E} = \mu\varepsilon \frac{\partial^2 \mathbf{E}}{\partial t^2} \tag{1.1}$$

$$\mu \ldots permeability \qquad \varepsilon \ldots permittivity$$

If it is assumed that the field only varies in one direction (often z), a plane wave solution can be found taking the form:

$$\mathbf{E}(z,t) = \mathbf{E}_0(t - \frac{z}{v}) \tag{1.2}$$

This solution represents a wave propagating in z-direction with a constant field in the

x-y plane. In the case of a pulsed laser $\mathbf{E}_0$ represents the pulse shape and $v = \frac{1}{\sqrt{\mu\varepsilon}}$ the propagation velocity. It is worth mentioning, that $\frac{1}{\sqrt{\mu_0\varepsilon_0}} = c$, and therefore the propagation velocity is $v = \frac{c}{n}$, if $\mu = \mu_0$ (corresponding to propagation in free space).

For the case of a sinusoidal solution, the equation takes the following form:

$$\mathbf{E}(z,t) = \mathbf{E}_0 cos(\omega t - kz + \phi) \tag{1.3}$$

$$\mathbf{E}(z,t) = Re\left\{\tilde{\mathbf{E}}_0 e^{j(\omega t - kz)}\right\} \tag{1.4}$$

$$\omega \ldots angular\ frequency \qquad k \ldots propagation\ constant \qquad \phi \ldots phase$$

$$with \quad k = \omega\sqrt{\mu\varepsilon} \qquad \lambda = \frac{2\pi}{k}$$

$$or\ in\ free\ space\ (\mu = \mu_0) \quad k = \frac{\omega n}{c} \qquad \lambda_0 = \frac{2\pi c}{\omega}$$

For real laser beams, which have finite transverse extent and are therefore not plane waves, a so called paraxial approximation can be found, which assumes a superposition of plane waves with propagation vectors close to the main direction of propagation (z-axis). [9, p. 4 : 10]

In this case, the wave equation can be approximated as:

$$\nabla_T^2 u + \frac{\partial^2 u}{\partial z^2} - 2jk\frac{\partial u}{\partial z} = 0 \tag{1.5}$$

One particular solution to this wave equation is called the Gaussian-beam solution, which describes the transverse variation of the beam-shape with $u(x,y,z)$ both for propagation in free space, as well as inside of a laser-resonator. Therefore, also all of the possible transverse laser modes result from this equation, whereas longitudinal Laser modes depend only on the geometrical dimensions of the laser cavity.

Below, some properties of the Gaussian-beam solution are given:

$$w^2(z) = w_0^2\left[1 + \left(\frac{z}{z_0}\right)^2\right] \tag{1.6}$$

$$z_0 = \frac{\pi w_0^2 n}{\lambda} \tag{1.7}$$

$$\frac{1}{R(z)} = \frac{z}{z^2 + z_0^2} \tag{1.8}$$

In this description w is the $\frac{1}{e^2}$ beam radius, w_0 is the beam radius at the focus, z_0 the so called Rayleigh-length, and R the radius of curvature of the phase-front. [9, p. 17 : 22]

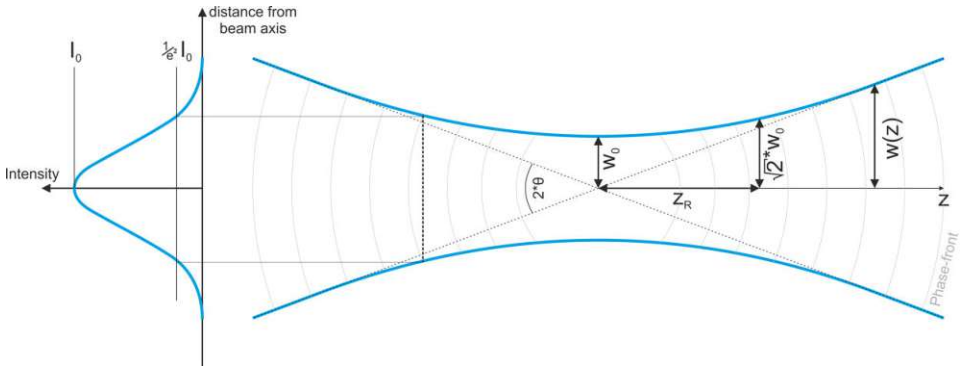

Figure 1.1: Illustration of the propagation of a Gaussian Laser-beam with the properties described by the paraxial approximation.

1.1.2 Generation of Laser Pulses

The simplest form of a laser cavity or resonator consists of a set of mirrors and a gain medium, which acts as an optical amplifier. To achieve optical amplification energy has to be *pumped* into the gain medium to elevate electrons to a higher energy state and achieve population inversion (more electrons in an excited energy state than in a lower one ⇒ higher probability of stimulated emission). For steady-state operation, first the gain has to balance out exactly the round-trip loss, which is also called the *gain condition*. The second condition, which has to be satisfied is the *phase condition*, which states that the Laser is only allowed to oscillate at certain discrete frequencies depending on the cavity length l, which are also called longitudinal modes. In other words, only standing waves with nodes exactly at the cavity mirrors are allowed:

$$m\frac{\lambda}{2} = l \quad \Rightarrow \quad m\frac{\frac{2\pi c}{\omega}}{2} = l \tag{1.9}$$

$$\omega_m = \frac{m\pi c}{l} \qquad f_m = \frac{mc}{2l} \tag{1.10}$$

$$\Delta f = \frac{c}{2l} \tag{1.11}$$

If multiple longitudinal modes are present in the output of a laser, it is called multimode operation (figure 1.2 a), and the opposite is called single-mode or monochromatic operation (figure 1.2 b). Single-mode operation can only be achieved, if a frequency-dependant loss element is inserted into the laser cavity.

In order to understand the operation of a laser, the gain-medium function has to be distinguished into *small-signal* and *saturated* gain. Small-signal gain is available even at

very low light intensities and is only dependent on the gain-medium and the pump level. As photons are amplified through stimulated emission, electrons of the gain medium fall back to their lower energy state, in other words by amplification stored energy is taken away from the gain-medium, and the gain is reduced. This is called the saturated gain and is dependent on the gain-medium properties, the pump level and the intra-cavity laser intensity. As long as the gain remains below the loss, no amplification is possible and therefore the laser intensity is zero.

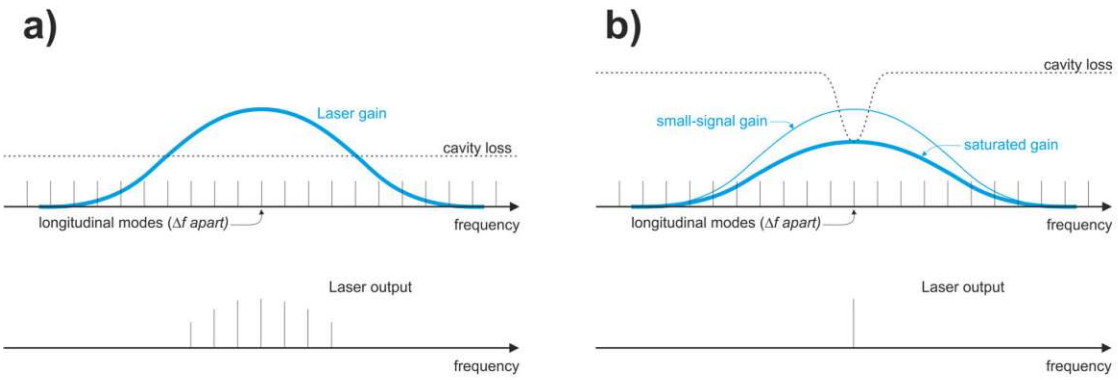

Figure 1.2: Figurative illustration of the working principles of a multimode (a), and a single-mode or monochromatic (b) Laser also showing the difference between small-signal and saturated gain.

Additionally, there is also a stability criterion for laser cavities. If we think of the simple form consisting of two mirrors with a gain medium between them, only the light traveling from one mirror to the other one, and afterwards only the reflected light towards the first one can be amplified and finally used. For a two-mirror resonator this stability relies solely on the geometry with R_1 and R_2 being the radii of the mirrors and d the distance between them:

$$0 \leq g_1 g_2 \leq 1 \tag{1.12}$$

$$\text{with} \quad g_1 = 1 - \frac{d}{R_1} \qquad \text{and} \qquad g_2 = 1 - \frac{d}{R_2} \tag{1.13}$$

If we take a look at the intensity profile of a multimode laser, there is no pulsed output, but a continuous one with random fluctuations around the average intensity, which is proportional to $N|E_0|^2$, where N is the number of modes oscillating inside the laser cavity. These fluctuations are periodic with a period $T = \frac{1}{\Delta f} = \frac{L}{c}$, see figure 1.3a.

The phases of all of the longitudinal modes are random, thus a random fluctuation around an averaged intensity value emerges. In contrast, if all of the phases are locked,

there is only one distinct point, for which one peak of every sinusoidal wave of the modes overlap and constructively interfere. Everywhere else, destructive interference happens and the peaks average out to approximately zero. This is also called *mode-locking* and will be discussed in further detail, a figurative intensity profile can be seen in figure 1.3b.

The output of such a mode-locked laser consists of short, periodic pulses with a peak intensity proportional to $N^2|E_0|^2$, where the averaged intensity is the same as for the output with random phases. The period of the pulses is $T = \frac{1}{\delta f}$. The pulse duration is limited by the bandwidth of the gain-medium and is approximately $\Delta t = \frac{1}{N} * \Delta f$, where N is the number of modes and Δf is the Laser bandwidth.

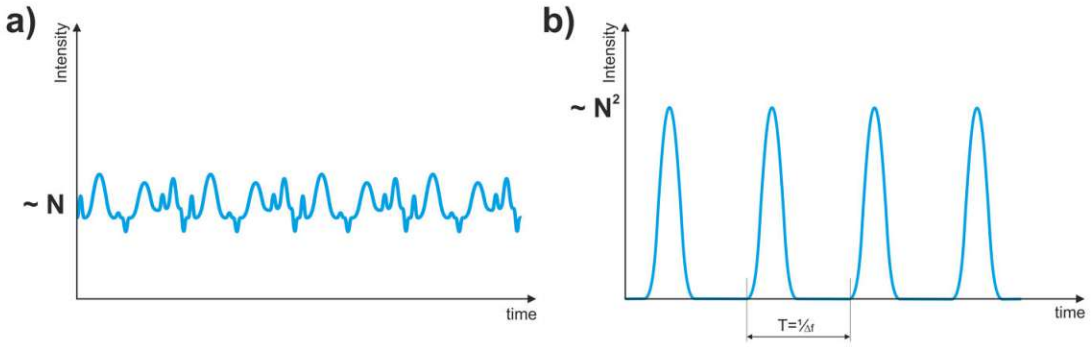

Figure 1.3: Figurative illustration of the intensity over time of the output of a laser with random phases of the modes (a), and a mode-locked laser (b). It can be seen that the peak Intensity of the mode-locked pulses is a factor N higher than the averaged output of the random phases.

The bandwidth limitation of the pulse duration can be traced back to Heisenberg's uncertainty principle, which can also be expressed as an energy-time uncertainty:

$$\Delta E \Delta t \geq \frac{\hbar}{2} \tag{1.14}$$

$$\text{with} \quad E = \hbar\omega = \hbar\frac{2\pi c}{\lambda} \quad \Rightarrow \quad \Delta\omega\Delta t \geq \frac{1}{2} \tag{1.15}$$

$$\hbar = \frac{h}{2\pi} \ldots \text{reduced Planck/Dirac constant}$$

The electric field of a multimode laser can be written as:

$$e(z,t) = Re\left\{\sum_m E_m e^{j(\omega_m t - k_m z + \phi_m)}\right\} \tag{1.16}$$

$$\text{with} \qquad \omega_m = \omega_0 + m\Delta\omega = \omega_0 + m * \frac{2\pi c}{L} \qquad \text{and} \qquad k_m = \frac{\omega_m}{c}$$

$$e(z,t) = Re\left\{a\left(t - \frac{z}{c}\right) e^{j\omega_0(t-\frac{z}{c})}\right\} \tag{1.17}$$

$$\text{with} \qquad a\left(t - \frac{z}{c}\right) = \sum_m E_m e^{j(m\delta\omega(t-\frac{z}{c})+\phi_m)} \ldots \text{envelope function}$$

$$\text{and} \qquad e^{j\omega_0(t-\frac{z}{c})} \ldots \text{carrier function}$$

This means that the the electric field is the product of an envelope function and a carrier function, which both travel at the speed of light, so the envelope function has a period proportional to the cavity length $T = \frac{2\pi}{\Delta\omega} = \frac{1}{\Delta f} = \frac{L}{c}$ [9, p. 10:15 and 22:24].

1.1.3 Mode-Locking

Mode-locking means that the phase relations of the different longitudinal modes are kept constant in order to achieve short laser pulses as already described above. Two principles of mode-locking can be differentiated in terms of how they interact with the laser cavity/pulse in active and passive techniques.

Active modulation refers to externally driven modulators, which influence the amplitude or the phase of the circulating pulse.

Passive mode-locking, on the other hand, refers to processes taking place inside the laser cavity without external interference. These processes can be self-amplitude-modulation (SAM) or self-phase-modulation (SPM), both being dependent on the properties of the circulating pulse, which is itself dependent on the modulation, therefore it is called a self-induced modulation.

Since the shortest pulses were generated with passive mode-locking and also most of the solid-state Lasers, which happens to be the type used in this thesis, utilize passive techniques, passive mode-locking will be discussed in further detail.

Passive Mode-Locking

As the self-modulation is an interaction between the Laser pulse itself and the cavity components, it is automatically synchronized with the cavity round-trip. One way of modulation is an optical component which acts as a nonlinear loss element, for example a saturable absorber. These modulation processes are the foundation for solid-state Lasers and were also utilized in organic-dye-lasers, which were used as standard ultrashort pulse generators for a long time.

Since the modulation is dependent on the pulse itself, a circulating laser pulse experiences a constant cavity loss and a time dependent loss and gain. Assuming that the pulse should be reproduced after 1 round-trip through the cavity and that the time-dependant loss and gain are small, one form of Haus's master equation for mode-locking can be derived:

$$\frac{d^2a(t)}{dt^2} - \delta T\omega_c \frac{da(t)}{dt} + [g(t) - l(t) - l_0]\,\omega_c a(t) = 0 \tag{1.18}$$

$\omega_c \ldots$ finite cavity bandwidth $\quad a(t) \ldots$ pulse envelope

$g(t) \ldots$ time-dependant gain $\quad l(t) \ldots$ time-dependant loss

$l_0 \ldots$ linear cavity loss $\quad \delta T \ldots$ time-shift due to nonlinear effects

In organic-dye-lasers mostly amplitude modulation was used for mode-locking in the form of different dyes which acted as saturable absorbers. These can be distinguished in terms of the relation between the relaxation time of the absorber (τ_A) and the pulse-width (t_p) into fast ($\tau_A \ll t_p$) and slow ($\tau_A \gg t_p$) saturable absorbers. For fast saturable absorbers the absorption decreases with increasing Laser power and therefore the wings of a pulse see higher losses than the peak, which leads to pulse-shortening.

The same is also true for a saturable gain medium, but the per pulse saturation is very small in the case of solid-state lasers and saturates more in response to the average power.

Real fast saturable absorbers are difficult to find, but a clever usage of another nonlinear optical effect acts as an artificial fast saturable absorber and leads to mode-locking in solid-state lasers. This effect is based on a nonlinear refractive index change, also called *optical Kerr effect*.

$$n = n_0 + n_2 I(t) \tag{1.19}$$

$$\text{with} \qquad I(t) = \frac{|a(t)|^2}{A_{eff}} \tag{1.20}$$

$$a(t) \ldots \text{pulse amplitude} \tag{1.21}$$

$A_{eff} \ldots$ effective beam area, e.g. for a gaussian beam $\dfrac{w^2\pi}{2}$

It can be seen that the laser pulse induces a change in the refractive index due to the instantaneous intensity, the response time is in the low femtosecond regime. Because of nonlinear effects SAM (self amplitude modulation) and SPM (self phase modulation) arise and one popular scheme using these effects to achieve mode-locking is the so called *Kerr lens mode-locking* (KLM). Due to the change in refractive index, the Kerr-medium

acts either as a converging or a diverging lens, which, combined with an aperture, alters the loss of the Laser cavity depending on the instantaneous intensity (see figure 1.4).

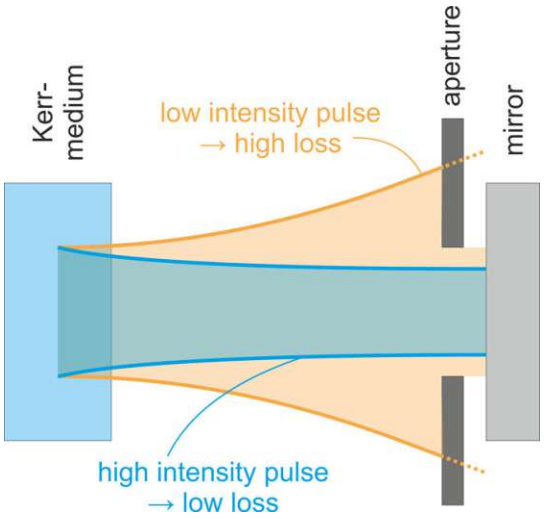

Figure 1.4: Illustration of *Kerr*-lensing for a high and a low intensity laser pulse. The phenomenon of the *Kerr*-medium acting as a converging lens in conjunction with an aperture is used in *Kerr lens mode-locking* (KLM), where the loss of the cavity is dependent on the laser pulse intensity.

In order to account for the nonlinear effects, the terms of equation 1.18 have to be rewritten. SAM can be modeled by writing the loss terms as:

$$l_0 + l(t) \approx l - \gamma |a(t)|^2 \tag{1.22}$$

$l \ldots$ constant loss $\qquad \gamma \ldots$ SAM coefficient

Light propagating through a nonlinear optical medium experiences an optical phase-shift $\Delta\phi(t)$, which is proportional to the intensity, and with $\Delta\phi(t) \approx -\delta|a(t)|^2$ the pulse envelope after the nonlinear medium ($a'(t)$) can be written as follows:

$$\Delta\phi(t) = \frac{-2\pi}{\lambda} n_2 I(t) L \tag{1.23}$$

$$a'(t) = \left[1 - j\delta|a(t)|^2\right] a(t) \tag{1.24}$$

$\Delta\phi(t) \ldots$ phase shift $\qquad \delta \ldots$ SPM coefficient

Such a phase-shift varying with time gives rise to time-varying frequency shifts away from the carrier frequency, for $n_2 > 0$ this leads to red shifts (lower frequency, higher wavelength) at the leading edge and blue shifts at the trailing edge of the pulse. This phenomenon is also called *chirp* (see figure 1.5), in the case described above *up-chirp*,

since the frequency increases with time.

Another effect that has to be considered is dispersion, which originates from differing round-trip times of different frequencies and can be an important pulse broadening mechanism. The propagation constant $\beta(\omega)$ can be expanded using a tailor series, which again can be used to model a change in spectrum $A(\tilde{\omega})$, where the first two factors can be ignored, since they can be interpreted as a constant phase shift and a constant delay. After Fourier-transform a useful expression for dispersion can be found as follows:

$$A'(\tilde{\omega}) = e^{-j\beta_0 L} e^{-j\beta_1 \tilde{\omega} L} e^{-j\frac{\beta_2}{2}\tilde{\omega}^2 L} A(\tilde{\omega}) \tag{1.25}$$

$$\Rightarrow A'(\tilde{\omega}) \approx \left(1 - j\frac{\beta_2}{2}\tilde{\omega}^2 L\right) A(\tilde{\omega}) \tag{1.26}$$

$$\textit{Fourier-transform} \quad \Rightarrow \quad a'(t) \approx \left(1 - jD\frac{d^2}{dt^2}\right) a(t) \tag{1.27}$$

$$D = \frac{\beta_2 L}{2} \ldots \text{dispersion coefficient} \qquad \beta \ldots \text{propagation constant}$$

$$\tau(\omega) = \beta_1 L + \beta_2 \tilde{\omega} L \tag{1.28}$$

As a consequence of dispersion, a frequency dependent delay $\tau(\omega)$ can be defined (equation 1.28), which means that for normal dispersion ($\beta_2 > 0$) shorter wavelengths propagate more slowly and are displaced towards the trailing edge ⇒ up-chirp (see figure 1.5).

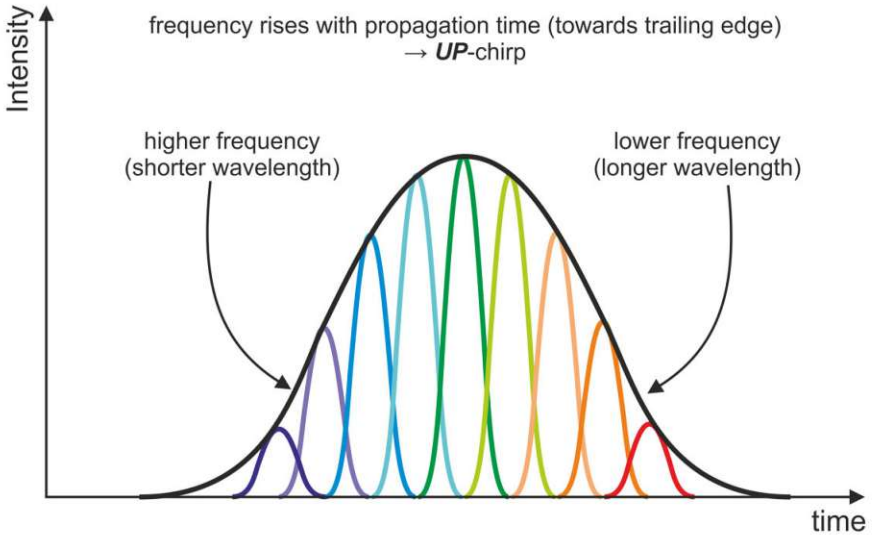

Figure 1.5: Illustration of the frequency shift in the carrier frequency of an *up*-chirped pulse.

Starting at Haus's master equation for mode-locking (equation 1.18), assuming that the main bandwidth limiting arises from the gain medium ($\frac{1}{\omega_c^2}\frac{d^2}{dt^2} \rightarrow \frac{1}{\Omega_g^2}\frac{d^2}{dt^2}$) and plugging in all of the new terms from equations 1.22 - 1.27, a new form of the mode-locking equation can be found, describing the changes of a pulse after one round-trip in the laser cavity:

$$a_{n+1}(t) = \left\{1 + g\left(1 + \frac{1}{\Omega_g^2}\frac{d^2}{dt^2}\right) - \left(l - \gamma|a(t)|^2\right) - j\delta|a(t)|^2 + jD\frac{d^2}{dt^2}\right\} a_n(t) \tag{1.29}$$

$\Omega_g \ldots$ half width at half maximum of the gain line

As stated before, for steady-state mode-locking, it is necessary that a pulse reproduces itself after one round-trip inside the laser (within a phase-shift Ψ). Also assuming again that the phase shift per pass is small, a solution to the mode-locking equation 1.29 in the form of a chirped secant hyperbolic can be found:

$$a_{n+1}(t) = a_n(t)e^{j\Psi} \approx a_n(t)(1 + j\Psi) \tag{1.30}$$

$$a(t) = a_0\left[sech\left(\frac{t}{t_p}\right)\right]^{1+j\beta} \tag{1.31}$$

Inserting this solution (equation 1.31) back into the mode-locking equation (equation 1.29), a set of two complex characteristic equations can be found, which, together with the gain saturation equation, can be solved simultaneously to find all of the unknown parameters a_0, t_p, β, g and Ψ.

$$g - l - j\Psi + \frac{(1 + j\beta)^2}{t_p^2}(D_g + jD) = 0 \tag{1.32}$$

$$(D_g + jD)\frac{2 + 3j\beta - \beta^2}{t_p^2} = (\gamma - j\delta)a_0^2 \tag{1.33}$$

$$g = \frac{g_0}{1 + \frac{\langle P\rangle}{P_G}} \tag{1.34}$$

$g_0 \ldots$ small signal gain $\qquad P_g \ldots$ gain saturation Power

$$\langle P\rangle = \frac{2a_0^2 t_p}{T} \ldots \text{ average laser power}$$

If there is no dispersion and no SPM, the behavior inside the laser cavity is equivalent to a laser cavity with a fast saturable absorber (for example a dye Laser). However, SPM can lead to new frequency components, which leads to a broader bandwidth and enables shorter pulses.

SPM and Dispersion both lead to *up-chirped* pulses, so if there is Dispersion and SPM

simultaneously, Group Velocity Dispersion (GVD) amplifies the down-shift of frequency components at the leading edge and the up-shift at the trailing edge of the pulse. This interaction yields pulses which spread faster and experience greater chirping, enabling pulse compression to shorter durations using chirp compensation outside of the Laser cavity. This chirped pulse compression forms the basis of the advent of solid-state lasers for ultrashort pulse generation and also led to the Nobel-prize for Donna Strickland and Gerard Mourou [8].

If the Dispersion is anomalous ($D < 0$), it leads to a down-chirp, while SPM still leads to an up-chirp, which makes it possible that the cavity can be tuned in order for no net chirping to occur yielding pulses called *Solitons*, which can propagate without temporal or spectral distortion and can therefore be used in optical communication systems. [9, p. 32:81]

To summarize ultrashort laser pulse generation, the parameters of the laser cavity, or in other words the coefficients of equation 1.29 have to be chosen in a way that stable mode-locking is assured and outcoupled laser pulses have the desired properties. Therefore, γ has to be greater than zero (SAM has to be present), in order to achieve a net gain window for the peak of a circulating pulse, with high enough loss on either side, so unwanted perturbations are not amplified and pulse-shortening can take place to a certain degree. Furthermore, if a nonlinear element is inside the cavity, δ and D (SPM and Dispersion) are present and therefore pulses will be chirped. This can be utilized to achieve either *Solitons* (equal in magnitude, but different sign of chirp), or even shorter pulses than with SAM alone via external pulse compression.

1.2 Deposition of Thin Films

One goal of this thesis was to achieve data storage by writing bits in a ceramic material via irradiation with femtosecond laser pulses. This data writing process was achieved by ablation of a thin ceramic coating on different substrates, acting as the 'data carrier'. In the following chapters, some background about the coating and the ablation process will be presented.

Coatings are considered as 'thin', if their thickness is 1 micron ($1\mu m$) or less. The processes to produce them can be differentiated by the type of coating material (e.g. organic, inorganic), the phase of the coating material (e.g. solid, liquid, gaseous), the deposition technique (e.g. mechanical, physical, chemical, thermal), or the process characteristics (wet: painting, dipping, electro-plating; dry: vapor deposition). Examples for typical, well established techniques are electroplating, chemical vapor deposition (CVD) and physical vapor deposition (PVD), which is the chosen method to produce the samples used in this thesis. The result of such a coating process is always the same system of a bulk material called substrate, a coating of a different material, and an interaction zone between them, see figure 1.6.

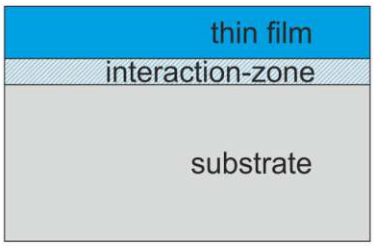

Figure 1.6: Illustration of a thin film system consisting of a bulk material (substrate), a coating of a material differing from the bulk (thin film), and an interaction zone between them.

1.2.1 Physical Vapor Deposition (PVD) - Sputtering

In vapor deposition the coating material is transported from the source to the substrate in form of a vapor, where it transitions to a solid phase by condensation, nucleation and growth. The generation of the vapor can be done with different techniques by a chemical or physical process, therefore CVD and PVD, where PVD can be divided further into evaporation, ion plating, and sputtering. The source of the coating material, which is vaporized during the process, is called 'target'.

All of the PVD-processes have in common, that they require a high vacuum environment of the target-substrate system, in order to avoid unwanted reactions and to minimize collisions of the transported, vaporized coating material. The quality of a

vacuum is given by the residual pressure present inside the vacuum chamber, which is measured in Bar (bar), Pascal (Pa), Standard Atmospheres (atm), or Torr (Torr). The SI-unit is Pascal, therefore the definitions for the other units are:

$$1\ bar = 10^5\ Pa$$

$$1\ atm = 101325\ Pa = 1.013\ bar$$

$$1\ Torr = \frac{1\ atm}{760} \approx 133.32\ Pa \approx 1.33\ mbar$$

Sputtering

In order to generate the vapor, which then forms the coating on the substrate, different techniques can be differentiated in thermal and physical ones. In contrast to thermal techniques, where the vapor is generated by heating, electric arcs or high energy beams, sputtering is a member of the physical techniques, where the vapor is generated by momentum transfer of bombarding particles.

This momentum transfer theory describes, that atoms from the target are ejected, because of the energy transferred to them in form of momentum from incoming bombarding particles. These particles are usually ions of a gaseous material and can therefore be accelerated by an electric field. The momentum transfer ejection (sputtering) leads to effects, which are unique for this process:

- the sputtering yield is rather insensitive to the target temperature, but it depends on the mass of the bombarding particles and their angle of incidence (AOI)
- a certain 'threshold energy' has to be reached in order for sputtering to take place
- sputtered atoms have high kinetic energies and are deposited in a ratio corresponding to the target bulk material, if it is an alloy

As the inert gas, typically Argon is used, because it is inexpensive and the ions are relatively heavy, which is important since the momentum transfer correlates with the mass of the bombarding particles. In order to quantify the effectiveness of the sputtering process, the sputtering yield is defined as:

$$Sputtering\ Yield = \frac{number\ of\ atoms\ ejected}{number\ of\ incident\ bombarding\ particles} \tag{1.35}$$

In order to accelerate the bombarding particles towards the target surface, it is common to ionize the inert gas and put the target to a negative bias potential. With this

plasma configuration positive gas ions are attracted and accelerated to the negative target surface, which they reach with an energy proportional to the potential drop.

Since there is a partial pressure of the inert gas present in the vacuum chamber, collisions and charge exchanges are inevitable, so there will always be a mix of ions and neutrals bombarding the target surface. A quantitative measure of how many collisions will happen is the mean-free-path, which is the average distance an atom, ion, neutral, or particle can travel without interacting with another one.

To generate and maintain a plasma, energy in the form of electrons has to be transferred to the inert gas in the region near the target surface. A very common way to maximize and sustain the plasma generation is to arrange a set of magnets and therefore apply a magnetic field, so electrons are kept near the target surface, or are even made to circulate on a closed path on it. This arrangement is called a magnetron and was also used to produce the samples for this thesis.

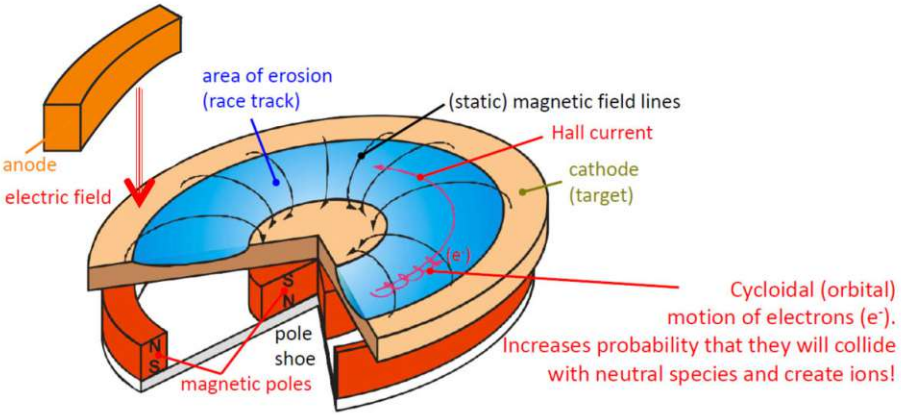

Figure 1.7: Illustration of a magnetron configuration in order to enhance gas ionization in the region of the target surface and therefore to optimize the plasma sputtering process. [7]

Because of the dense plasma in the region of the target surface, ions can be accelerated towards it in a higher quantity and at a lower potential, which results in a higher sputtering yield and a lower target heating. The disadvantage of this configuration is, that the plasma is mainly located where the magnetic field is the highest, so sputtering mainly occurs in that region and a so-called 'race-track' is formed because of the confined erosion. Because of this also the deposited film is dependent on the position of the substrate relative to the target.

Deposition of Alloys and Compounds

As mentioned before, the deposition of alloys is simple, since the film composition follows the one of the used target, as the target surface is removed layer by layer.

In order to deposit compound films, such as metal nitrides or metal oxides, also compound targets can be used, but in this case some of the gaseous constituent is lost in

transportation and condensation/reaction to or at the substrate surface. To overcome this phenomenon and achieve the desired compound film, quasi-reactive and reactive sputter deposition can be used.

In quasi-reactive deposition, the target itself is the compound desired to be deposited on the substrate and only a small partial pressure of reactive gas is used in order to make up for the aforementioned losses.

In reactive sputter deposition, the compound on the substrate is formed entirely from a reaction of the reactive gas with the depositing species from the target, e.g. a chromium target and a partial pressure of nitrogen form a CrN compound film on a substrate. In both cases the majority of the gas present in the vacuum chamber consists of the inert species with a high mass for the sputter process. With reactive sputtering care has to be taken and parameters have to be right to avoid target poisoning, which is the formation of a compound layer on the target surface, because this leads to a substantial decrease in sputter yield and a deviation from the desired compound composition. [6]

1.3 Ablation of Thin Films

Ablation of a material is defined as material removal from a surface area irradiated with laser light. This phenomenon is not a continuous process, but a highly nonlinear one, because the ablation only takes place, if a certain threshold is reached. In order to quantify this threshold, different methods and corresponding models have been suggested in literature, which start with the measurement of the ablated volume, depth, or area of the irradiated material. Subsequently, a series of these measurements is plotted against the energy used, in order to determine the threshold energy of ablation by extrapolating the gained data.

In order to keep values comparable and to be independent of the beam profile, and therefore also the Laser source, the threshold is given in units of energy over area called fluence, the most commonly used being $\frac{J}{cm^2}$ [1, 2]

1.3.1 Liu Curve, D**2 or (Squared) Diameter Method, D**2 - ln(E)

One of the simplest and quickest methods to determine the threshold fluence F_{th} is the empirical model suggested by J. M. Liu [5], which assumes a linear relation between the squared diameter of the ablation spot and the natural logarithm of the fluence. A plot of measured values and a linear fit can be seen in figure 1.10.

$$D^2 = 2 * w_0^2 * ln(\frac{F_0}{F_{th}}) \tag{1.36}$$

In this equation D is the diameter of the ablated spot, w_0 is the minimum waist radius of the Gaussian Laser beam and F_0 and F_{th} are the peak and the threshold fluence respectively, see also figures 1.8 and 1.9.

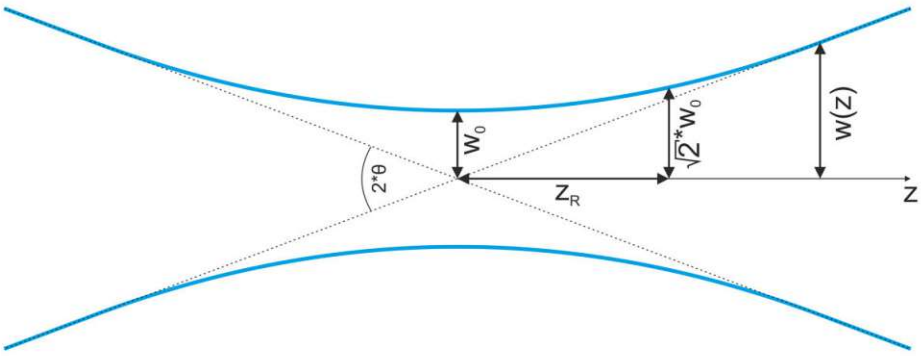

Figure 1.8: Illustration of the propagation of a Gaussian beam in axial direction (positive z direction). Here also the minimum waist radius w_0 and the definition of the Rayleigh length and the divergence angle θ can be seen.

Since it is assumed that the Laser beam has a Gaussian Intensity distribution, which

equals a perfect TEM_{00} mode, also the fluence has a distribution of the following power law, which is illustrated in figure 1.9.

$$F(r) = F_0 * exp(-2\frac{r^2}{w_0^2}) \tag{1.37}$$

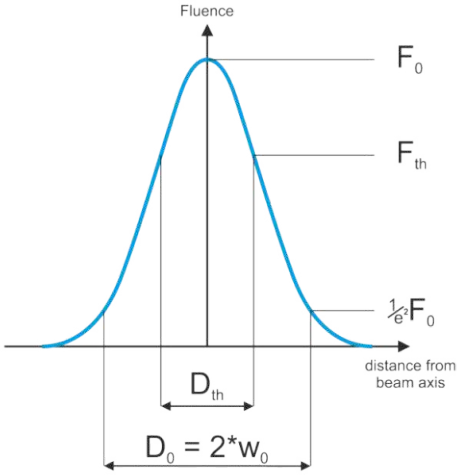

Figure 1.9: Illustration of the fluence distribution over the radial distance from the beam axis of a Gaussian beam, where the $\frac{1}{e^2}$ beam radius w_0 and the peak fluence F_0 can be seen.

As fluence is energy over an area, an area Integral of the Fluence distribution yields the pulse Energy E_p.

$$E_p = \int\int F(r)\ dA \tag{1.38}$$

$$E_p = \int_0^{2\pi}\int_0^{\infty} F_0 * exp(-2\frac{r^2}{w_0^2})\ r dr\ d\varphi \tag{1.39}$$

$$E_p = \int_0^{2\pi}\left[F_0 * \frac{exp(-2\frac{r^2}{w_0^2})}{\frac{-4r}{w_0^2}} * r\right]_0^{\infty} d\varphi = \int_0^{2\pi} F_0 * \frac{w_0^2}{4} d\varphi \tag{1.40}$$

$$E_p = F_0 * \frac{w_0^2\pi}{2} \quad \text{or} \quad F_0 = \frac{2E_p}{w_0^2\pi} \tag{1.41}$$

In other words, the peak fluence F_0 is the pulse energy E_p over the effective beam area (EBA) $\frac{w_0^2\pi}{2}$.

In the last equation, equation 1.41, it can be seen that the fluence and the pulse energy have a linear correlation, which means that equation 1.36 is also true for E_{th}. This leads to the fact, that with one set of experiments/measurements both the threshold Fluence F_{th} and the Gaussian beam diameter $2 * w_0$, which are unknown, can be determined at

once from the interception with the x-axis and the slope of a linear fit through the data points, respectively. Mathematically formulated, the determination of F_{th} and w_0 from the Liu-model follows from equation 1.36.

$$D^2 = k * ln(F_0) + d \tag{1.42}$$

$$k = 2 * w_0^2 \qquad \text{and} \qquad d = -2 * w_0^2 * ln(F_{th}) \tag{1.43}$$

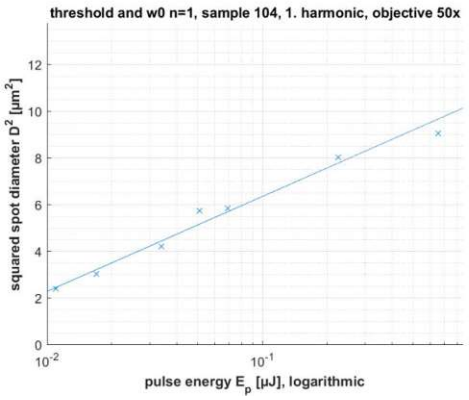

Figure 1.10: Brightfield microscopy image of a series of ablation spots on the left and the corresponding plot of of the squared diameters of the spots over the natural logarithm of the pulse energy on the right. For the spots in the left image in x direction the number of applied pulses and in y direction the pulse energy is varied. The plot on the right shows markers at the measured values and a linear fit through them for one applied pulse per ablation spot.

In figure 1.10 the procedure for the determination of w_0 and F_{th} can be seen. The image on the left shows ablation spots created with a different number of applied Laser pulses, and also different pulse Energies per spot. The plot on the right shows markers at the measured values of the squared diameters and the pulse Energies used corresponding to the ablated spots with one applied Laser pulse each. Also, a linear fit through this data is shown, which can then be used to calculate the Gaussian beam diameter $2 * w_0$ and the ablation threshold fluence F_{th}, as described in equations 1.42 and 1.43.

1.3.2 Incubation

There are many factors influencing the ablation threshold, e.g. laser wavelength, pulse duration, coating material, the number of pulses applied to the same spot, and the pulse rep.-rate. With increasing numbers of pulses per spot it can be observed, that the ablation threshold either in- or decreases, which is called incubation effect. Most materials respond with a decreasing threshold fluence $F_{th}(N)$.

It is not fully understood, which mechanisms are responsible for this behavior, so different explanations and models have been suggested. Physical processes could be an increase in absorption, due to ripple formation or the occupation/creation of laser induced material states, or a decrease in the specific damage energy, due to laser-induced defects or nano cracking. A simple, empirical model assumes an exponential relation between F_{th} and the number of applied pulses. [1, 3]

$$F_{th}(N) = F_{th}(1) * N^{S-1} \tag{1.44}$$

In this model S, or sometimes called ξ, is the so called incubation coefficient, which describes the incubation behavior of the material ($S = 1$ meaning no incubation). Therefore, both measured values, F_{th} and N, can be plotted logarithmic and afterwards the incubation coefficient (exponent in equation 1.44) can be determined by a linear fit through these data points (see figure 1.11).

Combined with the Liu-method described before, with one set of experiments first the ablation thresholds and the Gaussian beam diameter, and afterwards the incubation coefficient can be determined.

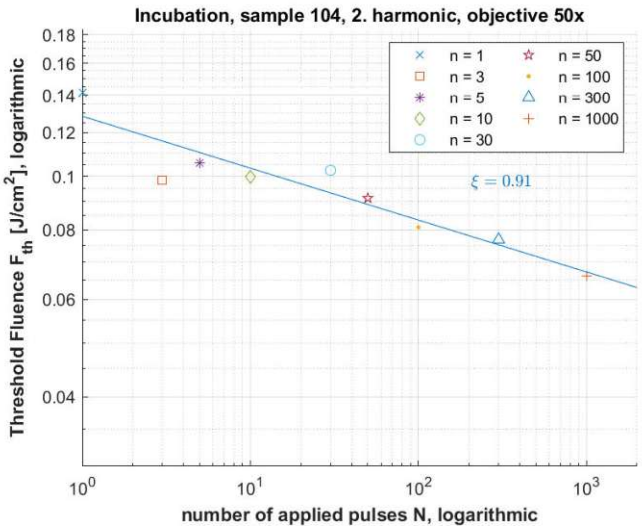

Figure 1.11: Plot of the threshold fluences F_{th} for different numbers of applied laser pulses per spot over the number of pulses with a linear function fitted to the data points. The incubation coefficient, determined from the linear fit, can be found in the upper right corner below the figure legend.

In figure 1.11 the experimentally determined threshold fluences are plotted against the number of applied pulses per spot. Furthermore, a linear function was fitted to the data, which allows to calculate the relation of F_{th} to the number of applied pulses in form of the incubation coefficient ξ with the help of equation 1.44:

$$ln(F_{th}(N)) = c_1 * N + c_2 \tag{1.45}$$

$$c_1 = S - 1 \quad \text{and} \quad c_2 = ln(F_{th}(1)) \tag{1.46}$$

2 Experiments

2.1 Experimental Setup

All of the following experiments were conducted on a commercially available, state of the art femtosecond micro-machining workstation, constructed and built by the lithuanian company *Workshop of Photonics* (WOP). The machine was designed specifically for the intended research on ablating spots with small diameters, using different wavelengths, different focusing optics and different materials, as well as for the inspection of the craters using a built-in microscope.

The laser source of this workstation is a femtosecond laser[1] with an attached harmonics generator module[2] in order to conduct experiments with wavelengths of 1030, 515 and 343 nm, respectively. This laser is capable of a maximum pulse energy of 84 μJ at a repetition rate of 60 kHz and a minimum pulse duration of 224 fs.

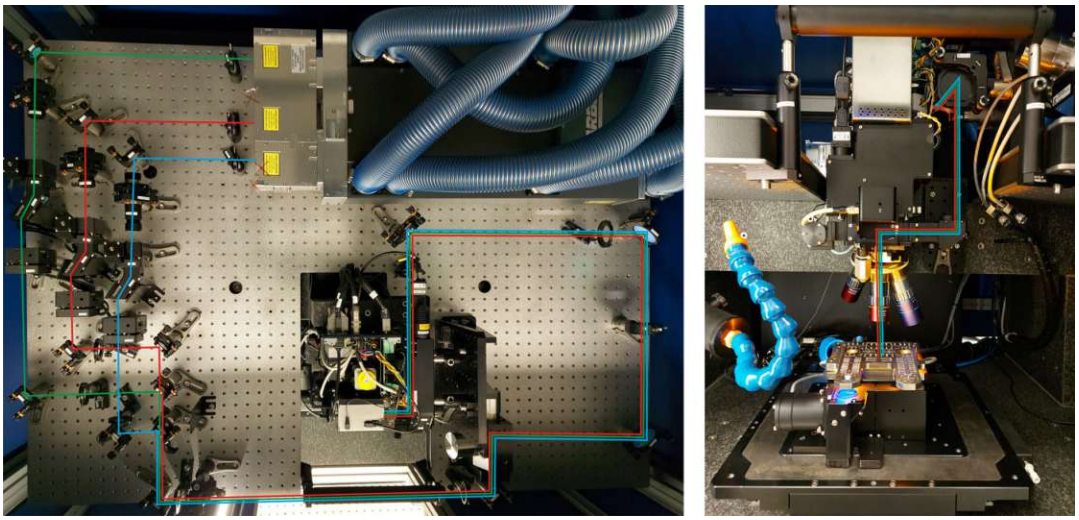

Figure 2.1: Image of the optical setup inside of the WOP micro-machining workstation from the top and from the front with an overlay of the beam paths of all of the laser harmonics. On the right it can be seen that the microscope and the laser share the last part of the path, which ends with the microscope objective.

The remarkable feature of this specially designed variant of the commercially available

[1] CARBIDE, *LightConversion* (CB5-05-0083-10-AM)
[2] (CBM03-2H-3H)

workstation is the machining head, in this case a confocal microscope[3], which allows manual and even automated inspection of ablated spots on a sample without the need to move the sample to an external device. The laser path and the microscope path are combined inside the microscope head and share the microscope objective (see figure 2.1).

In order to secure samples inside of the machine there is a sample-holder with an universal hole and channel pattern and an attached vacuum pump, which sucks flat substrates to its surface.

To reach different locations on the sample, there are 2 possibilities. The first one is a mechanical XYZ-stage[4], which has a travel range of 200 *mm* in X and Y and 5 *mm* in Z (see fig. 2.2 for the directions of movement).

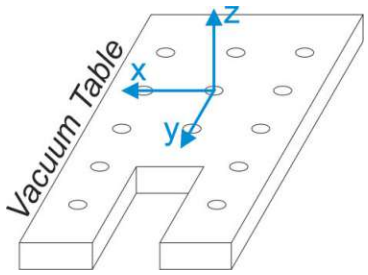

Figure 2.2: Directions of the moving directions of the stage. These directions were chosen for an intuitive actuation by the user (positive X = right arrow key → Laser moves to the right on the sample surface).

The second possibility is a galvanometer-, or short galvo-scanner (AGV in figure 2.3), which is a set of 2 actuated mirrors that are able to scan the Laser beam over the sample surface by rotating its mirrors without the need to move the sample.

The last components worth mentioning are a continuously variable attenuator (ATT 1" in figure 2.3) and a polarization rotator (ROT 1" in figure 2.3). The attenuator basically consists of a $\frac{\lambda}{2}$-plate and a polarizing filter and therefore transmits only a certain percentage of the Laser light. The polarization rotator is basically a $\frac{\lambda}{2}$-plate mounted in a rotation mount.
All of the coated samples were produced at a neighboring institute at the TU Vienna[5], Univ.Ass.Dipl.-Ing. Balint Hajas and Univ.Ass.Dipl.-Ing. Erwin Peck) using the PVD process described in a section 1.2.

[3] S-Neox, *Sensofar*
[4] *Aerotech* (PlanarDL-200XY-M1-E1-CMS1-PL3-TAS + ANT130V-5-CN1-PL2-TAS)
[5] E308 Institute of Materials Science and Technology, E308-01-1 Research Group for Thin Film Materials Science of Univ.Prof.Dipl.-Ing.Dr.mont. Paul Heinz Mayrhofer

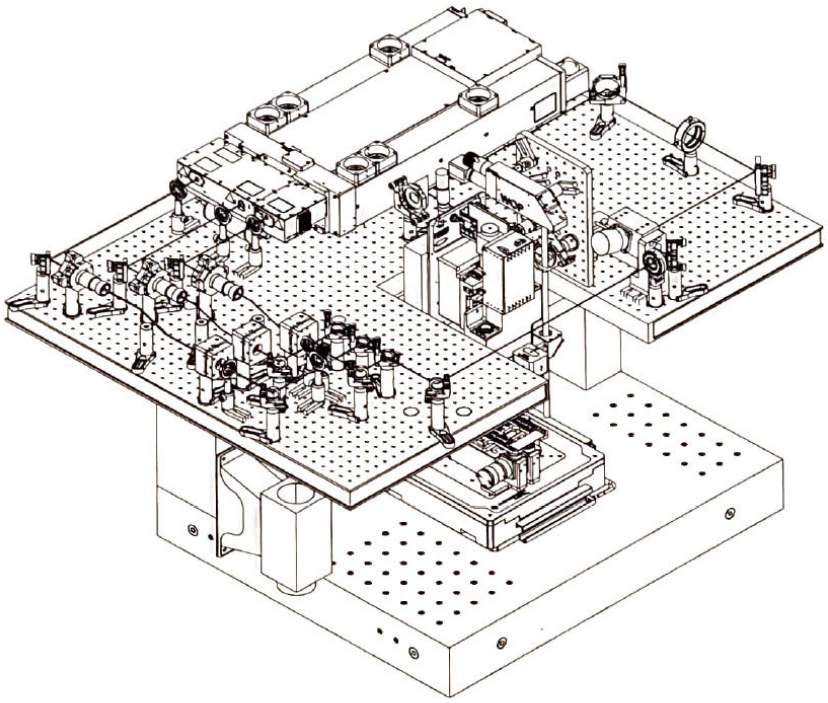

Figure 2.3: CAD drawing of the micro-machining workstation used to conduct the experiments of this thesis.

2.2 Initial alignment

Since the workstation was unique and only recently set up at the laboratory, some alignment and initial testing was necessary in order to ensure a good working condition and to get to know the machine and its capabilities.

When using the machine a misalignment of the sample holder was noticed, since both the machine vision and the built-in microscope were getting out of focus when the stage was moved. Therefore an iterative alignment process was conducted: starting in one corner of the sample holder, the machine vision was focused, then the stage was moved to another corner, where the height of the sample holder was adjusted via a set-screw until its surface was in focus again. This procedure was repeated iteratively until all of the corners of the sample holder were in focus of the machine vision within an acceptable tolerance.

Afterwards, an algorithm in the controlling software of the workstation (SCA) was programmed to measure the topology of the sample holder. The stage was moved to a defined set of points on the sample holder (see figure 2.4 a), where an autofocus routine, which is a built in feature of the software, was executed.

This routine finds the focal plane of the machine vision by varying the distance between the sample and the microscope objective in Z-direction, while running image processing. After this focusing the coordinates (x, y, z) of the stage were saved to a text file, so the

variation of the sample holder in Z-direction can be associated with the measurement points. The results of this measurement can be seen in the plots of figure 2.4.

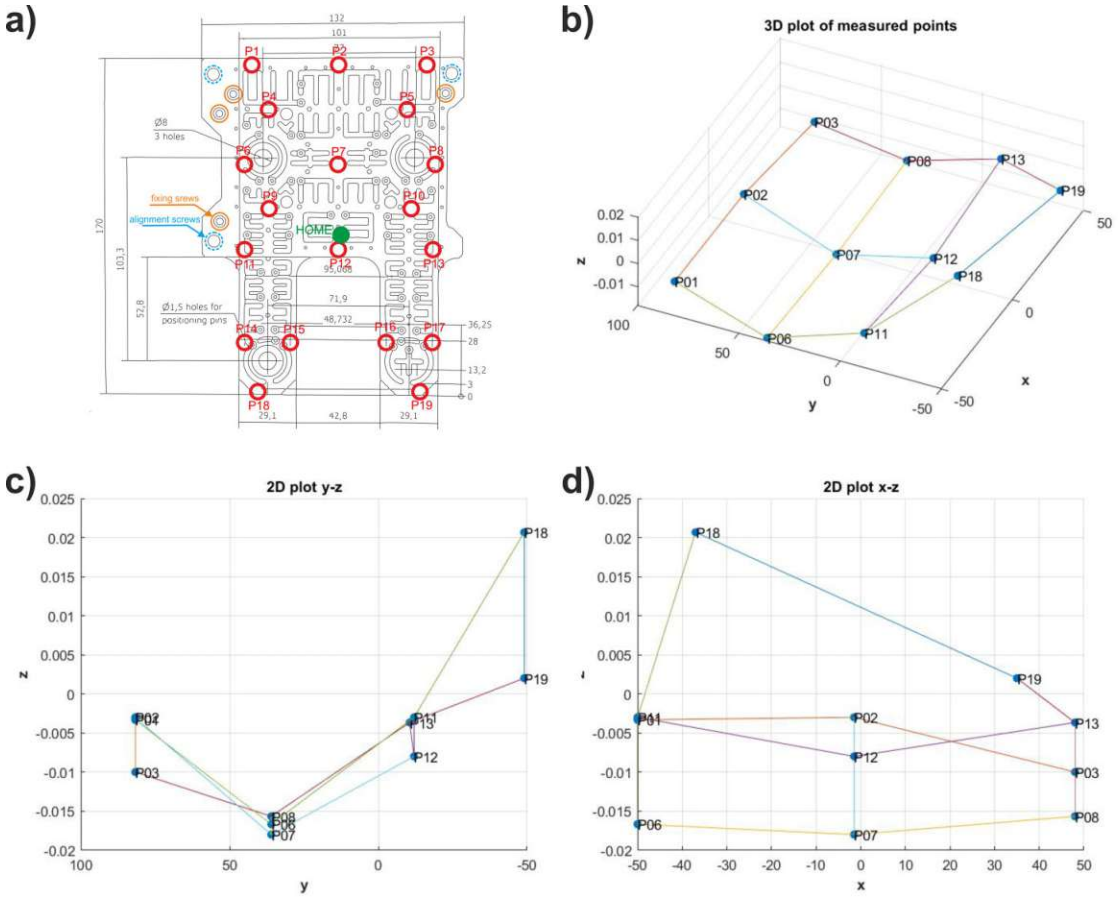

Figure 2.4: Plot of the measurement of the surface of the vacuum sample holder at various points. a) positions of the measurement points on the sample holder, b) 3D plot of the measured values, c) side- and d) front-view of the 3D plot. Values on the axis of the plots in *mm*.

Unfortunately, due to the construction of the sample holder (fixing screws besides the adjustment screws), there is an unavoidable bending moment applied to the aluminium plate, which leads to a low spot in the middle of the plate and high spots at the end of the "forks" (see plot c) of fig. 2.4). The variation in the X-direction resulted in a total difference of around 10 μm over the width of the sample-holder, which is acceptable, since the anticipated areas of interest in one experiment are small and therefore the deviations in Z-direction are negligible.

Another preliminary experiment was to check, if the focal planes of the laser and the machine vision matched or to quantify the difference, in order to account for it in following experiments.

To determine this possible offset, again, an algorithm was programmed. Again, it started with the built-in autofocus routine and set the starting point for the following

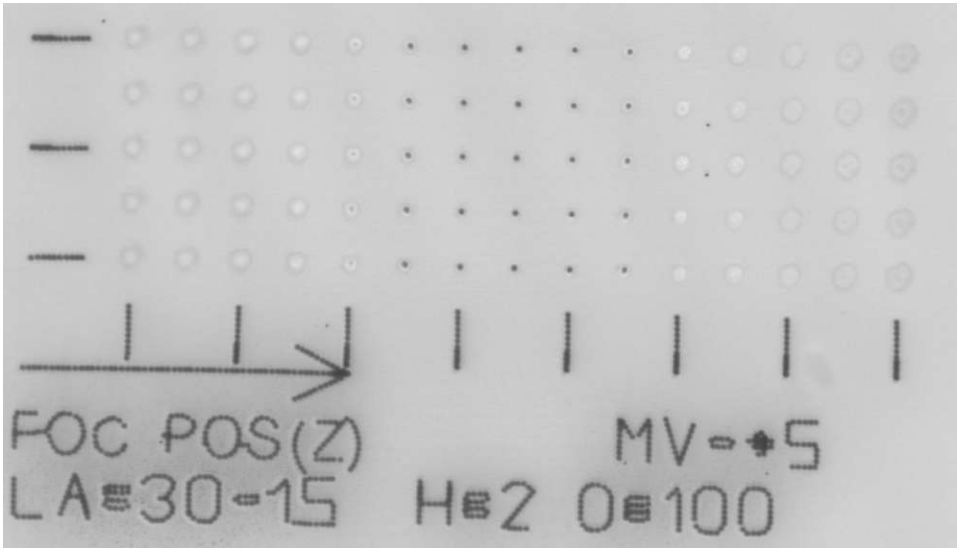

Figure 2.5: Brightfield image of one experiment to determine the offset between the focal planes of the Laser relative to the machine vision. The algorithm was carried out line by line. In this case, the second harmonic of the Laser (515 nm), the 100x objective and a delta of 5 μm was used.

z-coordinates. Then the stage moved to the starting point (x, y, z) triggered 1 laser pulse, moved a defined step in x and z, triggered a laser pulse, moved a defined step again, etc. This routine looped through a range in z of $z_0 \pm \Delta$, where z_0 was set at the beginning by the autofocus routine.

In each of the experiments to determine the difference between the focal planes of the laser and the machine vision, there are 5 lines of the step - trigger laser - step approach and all of the experiments were conducted for every combination of wavelength and suitable microscope objective at multiple positions on the same sample of CrN on a glass substrate.

After the algorithm was finished, a brightfield image was taken with the microscope (see figure 2.5) and then all of the ablated craters were measured. The average of the measured crater diameters at each X-position was then plotted and a polynomial of 2^{nd} degree was fitted to the central region. The plot corresponding to the experiment of fig. 2.5 can be seen in fig. 2.6.

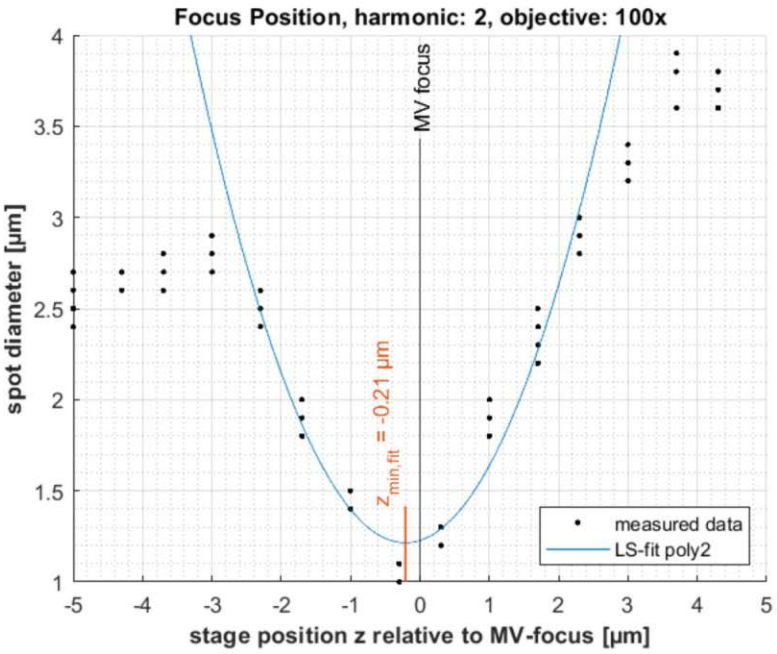

Figure 2.6: Plot of the average of the measured crater diameters of the focus-position-algorithm versus the relative z-position of the stage. In this case, the second harmonic of the laser (515 nm), the 100x objective and a delta of 5 μm was used.

As there was quite some deviation of the measured diameters of the ablated spots to the fit at the outer regions of the plots, only the central region of the values was considered in the least-squares fit. The Z-position of the minimum of the fitted curve was then taken as the "true" focal plane of the laser and therefore the relative difference to the machine vision or autofocus plane could be calculated (see table 2.1).

μm	1^{st} harm. (1030 nm)	2^{nd} harm. (515 nm)	3^{rd} harm. (343 nm)
10x NIR	-9.13	-3.92	-
50x NIR	-1.01	-0.26	-
100x NIR	0.05	-0.21	-
50x NUV	-	0.93	0.6

Table 2.1: Values of the difference between the focal planes of the laser to the machine vision in μm, derived from curves fitted to the measured crater diameters similar to fig.2.5+2.6.

The determined relative difference of the focal planes was used in later experiments as a fixed offset from the machine vision autofocus, in order to ensure ablation at the "true" focal plane.

2.3 Determination of Ablation Thresholds

As already described above, one goal of this thesis was to optically store data on a thin film sample consisting of a substrate and a coating, both made of a suitable material. Because preliminary tests already yielded promising results with CrN as the coating material, in this thesis coatings of the Cr-family were chosen to be investigated. A list of all of the coating materials and their corresponding thicknesses and substrates can be seen in table 2.2.

thickness ↓ / material →	Cr	CrN	Cr_2O_3	CrB_2	$AlCrN$
1000 nm	Sa/Cer	Sa/Cer	Sa/Cer	Sa/Cer	Sa/Cer
100 nm	Sa/Cer	Sa/Cer/G	Sa/Cer	Sa/Cer	Sa/Cer/G
25 nm	Sa/Cer	Sa/Cer	Sa/Cer	Sa/Cer	Sa/Cer
10 nm	–	G	–	–	G

Table 2.2: Combinations of different substrates, coatings and thicknesses which result in the samples used in this thesis. Sa: sapphire, Cer: ceramic, G: glass

The samples were produced at the Research Group for Thin Film Materials of the Institute of Materials Science and Thechnology of the TU Vienna by PVD. In the PVD vacuum chamber there was space for more than one substrate, so there were always 4 samples produced at the same time. A list of the samples that were tested during this thesis and their corresponding number can be found in table 2.3.

Sapphire / Ceramic	Cr	CrN	Cr_2O_3	CrB_2	$AlCrN$
1000 nm	10/14	18/22	26/30	38/42	46/50
100 nm	58/59	63/67	71/75	79/83	87/91
25 nm	96/100	104/108	112/116	120/124	128/132

Table 2.3: Numbers of the samples that were tested and their respective combination of coating material, thickness of the coating, and the substrate (sapphire/ceramic).

All of the samples of table 2.3 were tested in the same manner to determine the ablation threshold in the first place, and afterwards identify the combinations best suited for further research in terms of optical storage capabilities and smallest possible feature sizes.

The first step was to define an algorithm for the micromachining workstation, which allows to derive the $D^2 - ln(E)$/Liu curve in order to calculate the ablation threshold, which is described above (1.3.1). As the workstation is not only capable of automated

Figure 2.7: Brightfield image of one ablation threshold experiment, where the general approach of varying the laser pulses on the X-axis and the laser pulse energy on the Y-axis can be seen. At the bottom additional information about the sample number (S104), the laser harmonic (H=2) and the microscope objective (O=50) was inscribed. Labels on the Y-axis are in percent (laser attenuator - external attenuator), labels on the X-axis are the number of laser pulses (1, 3, 5, 10, ...).

laser pulsing, but can also write text and other formats directly onto the sample, all of the samples were given a number for later reference and the axes of the ablation threshold tests were labeled with the corresponding number of pulses and the parameters of the laser (laser attenuator - external attenuator (%), see fig. 2.7)

Directly after these experiments the power at each parameter step (see Y-axis in fig. 2.7) was recorded and used later to calculate the laser pulse energy via the repetition rate of the laser source:

$$\text{pulse energy } E_p = \frac{\text{Power } P}{\text{rep.-rate } f} \qquad (2.1)$$

$$\mu J = \frac{mW}{kHz}$$

The ablation craters could then be investigated with the built-in Sensofar microscope, which is also capable of the measurement of the diameters of these craters. With the measurements of the ablation craters, the corresponding pulse numbers and pulse energies, the data points could be plotted and a least-squares curve could be fitted. A plot of the measured crater diameters and the linear fits to this data corresponding to the experiment of figure 2.7 can be seen in figure 2.8.

After the first tests it was soon realized that the Liu-model does not fit to all of the data points in the chosen parameter range. In fig. 2.8 it can be seen that the data points

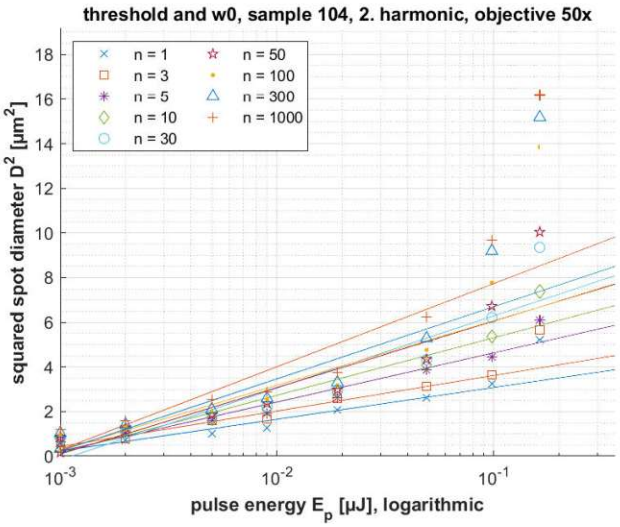

Figure 2.8: Plot of the measured squared ablation crater diameters and the corresponding logarithm of the pulse energy of one ablation threshold test of 25 *nm* CrN on Sapphire. Data corresponding to the test in fig. 2.7

at higher pulse energies do not follow the initial linear trend, especially for higher pulse numbers. In the individual plots for the number of pulses $n = 1$ and $n = 1000$ it is even clearer, that for higher pulse numbers there seems to be a kink, where the initial linear trend does not fit to the data points anymore, and a new trend seems to develop (see fig. 2.9).

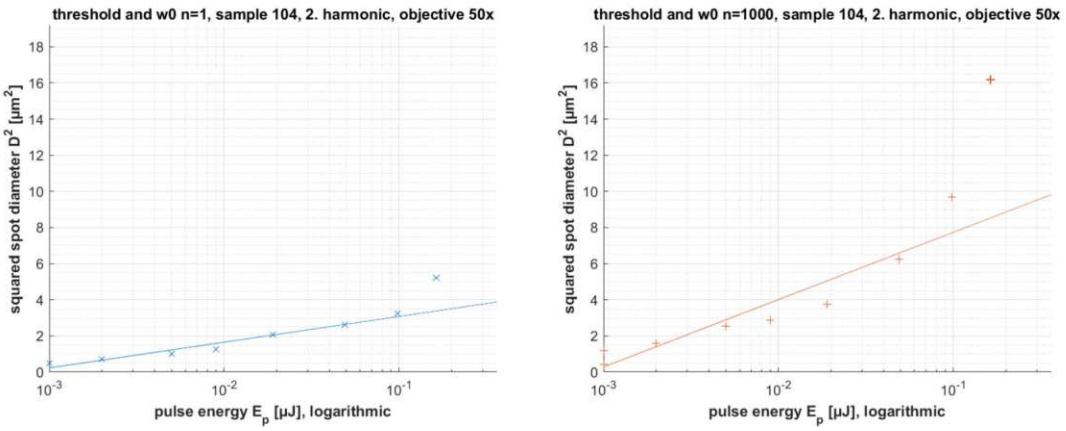

Figure 2.9: Individual plots corresponding to fig. 2.8 for a number of pulses of $n = 1$ on the left and $n = 1000$ on the right. At higher pulse numbers there seems to be a kink in the initial linear trend.

Due to the non-fitting model for higher pulse numbers and higher pulse energies, and because of the impracticality of high pulse numbers in a possible application as data storage, the algorithm for the ablation threshold test was modified. In the following

results, the number of pulses was chosen to vary from 1-5 (see image on the left of fig. 2.10).

In the plot on the right of figure 2.10 there is still some deviation from the linear trend present, again, especially for higher pulse numbers and pulse energies. Otherwise, the fitted curves seem to be more parallel, which would be more consistent with the assumed mathematical model, since the slope of the fitted curves corresponds to the minimum laser beam diameter at the focal spot, which is constant for the laser beam plus the used optics, and independent of the experiment or the number of pulses.

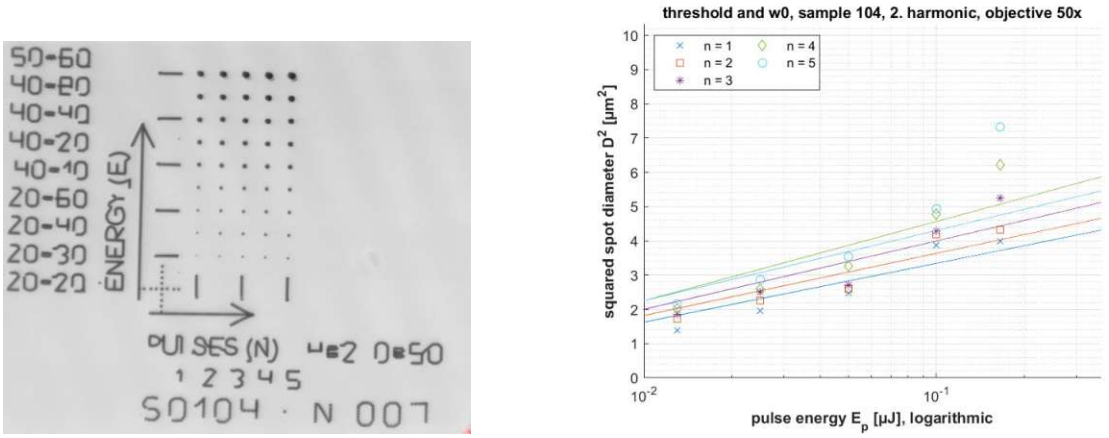

Figure 2.10: Brightfield image of the new ablation threshold experiments with a lower range of applied pulses per spot on the left. Plot of the measured squared ablation spot diameters over the logarithm of the applied pulse energies and corresponding fitted Liu-curves on the right. The sample is the same as the one in the corresponding experiment in figure 2.7.

The adjusted experiment was then conducted on all of the samples of table 2.3, the diameters of the ablation craters as well as the pulse energies were acquired and this dataset was then evaluated and further processed.

Since every dataset is unique and there seemed to be deviations from the predicted linear behavior as well as seemingly statistical outliers, a single plot for every number of applied pulses was created. In the course of plotting the data, the range of datapoints for the fit was adjusted, in order to achieve a best approximation of these points with the fitted Liu-curve.

After fitting the data points as described in section 1.3.1 to the equation 1.36

$$D^2 = 2 * w_0^2 * ln(\frac{F_0}{F_{th}})$$

the desired values for the Gauss-radius of the focal spot w_0 and the pulse energy corresponding to the ablation threshold can be calculated from the slope of the fitted curve and its interception with the X-axis (where $d = 0$) respectively. Furthermore, because the fluence relates linearly to the pulse energy, the threshold fluence can be calculated by dividing the threshold energy by the effective beam area.

$$F_{th} = \frac{E_{th} * 2}{w_0^2 * \pi} \tag{2.2}$$

E_{th}, w_0 . . . from fitted curve $\qquad \frac{w_0^2 * \pi}{2}$ . . . effective beam area

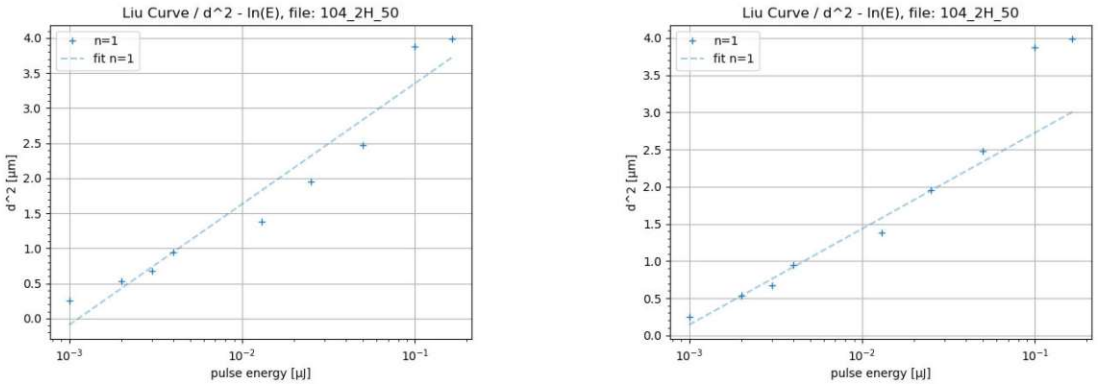

Figure 2.11: Plot of the fitted curves and the data points corresponding to the experiment in figure 2.10. On the left all of the data points were used in the least-squares fit, on the right the range of data points was adjusted.

There could be a number of reasons why not all of the measured crater diameters fit the Liu-model. One of them could be, that with higher pulse energies and applied pulse numbers the influence of the substrate increases, or that with changing laser power the harmonics generation contributes to slightly changing beam diameters. Another one could be, that the measurement of the diameters is not accurate enough, since the craters get more elliptical in shape and the affected zone surrounding them increases (see fig. 2.12).

Figure 2.12: Image of a measurement of the ablation crater diameter corresponding to the most right column of spots in figure 2.10. On the left, the measurement of the first spot from the bottom can be seen, on the right the last spot is depicted.

Because of the aforementioned reasons and due to the fact that only one experiment

and therefore measurement was conducted per sample, the work in this thesis aims for a preliminary selection of the best suited system for data storage. In order for statistically more reliable results more data has to be collected and further research and measurements have to be done.

In order to legitimate the conducted measurements and the parameters calculated from this data, the Gaussian beam radius in the focal plane can be approximated and then compared to the experimentally determined one. In order to do this approximation, factory provided data for the beam quality and the well-known M^2 formula can be used (2.3).

$$M^2 = \frac{\Theta \pi \omega_0}{\lambda} \tag{2.3}$$

$$\text{with} \quad \Theta \approx \frac{\text{radius of the beam } r}{\text{focal lenght of lens } f}$$

$$\omega_0 \approx \frac{\lambda}{\Theta \pi} M^2 \approx \frac{\lambda * f}{r * \pi} M^2 \tag{2.4}$$

$$M^2 = 1.05 \ , \ \lambda = 515 \ nm \ldots \text{factory provided data}$$

$$r = 1 \ mm \ldots \text{measured} \qquad f = 4 \ mm \ldots \text{Mitutoyo 50x}$$

$$w_0 \approx 0.7 \ \mu m \tag{2.5}$$

Plots of the measured Gaussian beam radii can be found in figure 2.13, where the markers indicate the average value and the error bars show the range of the minimum to the maximum value of ω_0.

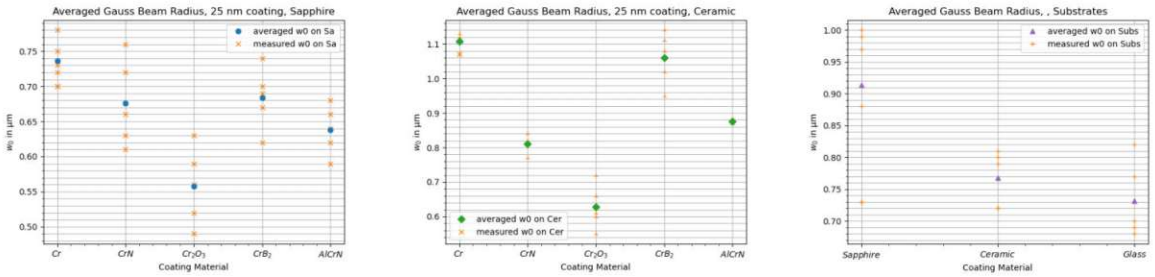

Figure 2.13: Averaged minimum Gaussian beam radii of the focal spot w0, determined by the experiments on the different coating materials with 25 *nm* on sapphire (left), ceramic (middle) and the substrates without coating (right). The orange asterisks represent the values calculated from the experiments.

The values of ω_0 vary significantly ($\pm$ 10 % of the average), however some of them do

match with the approximation of equation 2.5. This uncertainty in the beam diameter does also lead to an uncertainty in the threshold fluence, since the effective beam area is needed there. Because of this, in the discussion of the ablation thresholds both the threshold fluence, as well as the threshold energy should be considered and the fluences can be seen as qualitative indication only.

However, in order for a preliminary evaluation of all the samples mentioned in table 2.3, experiments and evaluations were conducted as described above, both for all of the samples, as well as for the substrates alone. The resulting ablation thresholds can be seen in the plots of figures 2.14 + 2.15.

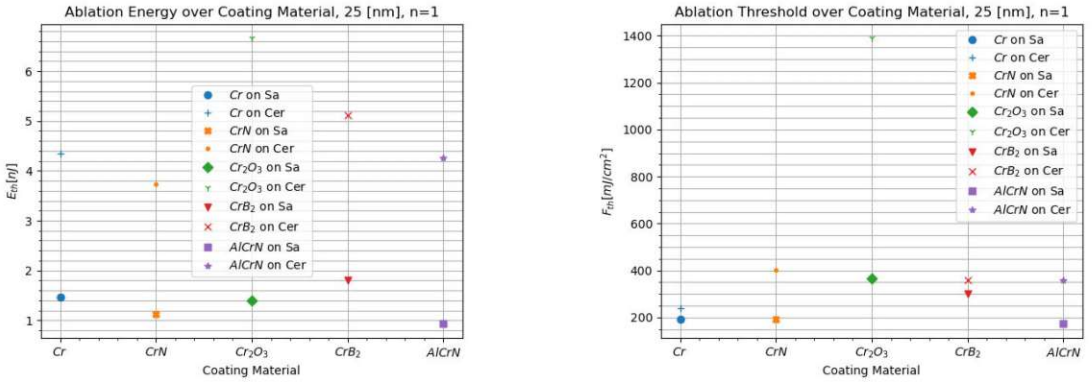

Figure 2.14: Plot of the ablation threshold energy (left) and the ablation threshold fluence (right) of all of the coating materials with a thickness of 25 *nm* on both substrates (sapphire and ceramic), determined by the experiment described above.

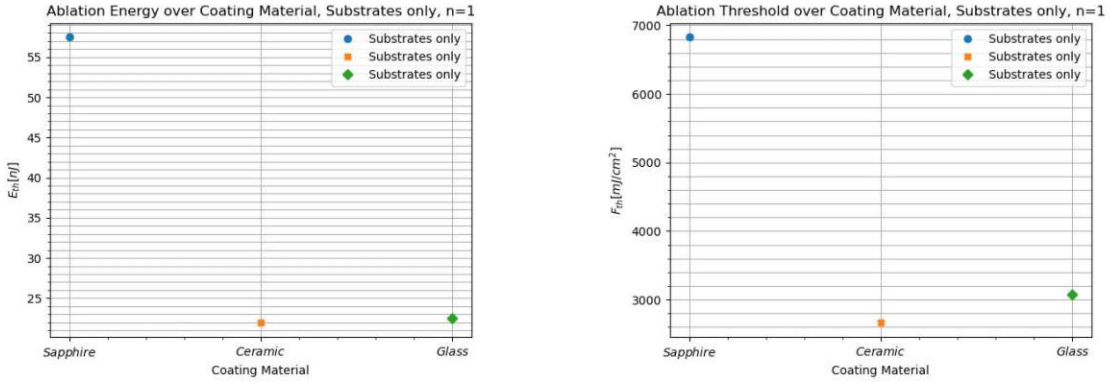

Figure 2.15: Plot of the ablation threshold energy (left) and the ablation threshold fluence (right) of the substrates used for the tested samples, determined by the experiment described above.

The coating thickness of 25 *nm* was chosen for this exemplary plot, because thinner coatings should yield better results of the Liu-fit, since the model assumes the threshold, where the ablated crater diameter reaches 0 at an infinitely small depth.

2.4 Parameters Influencing the Ablation Threshold

As the experiments were conducted on all of the relevant substrate-coating combinations, the data of the measurements as well as the threshold calculations could then be processed further in order to approach initially proposed questions as:

- How does the ablation threshold change with the number of applied pulses?
- How does the ablation threshold depend on the coating thickness?
- Does the ablation threshold depend on the the substrate?
- How does the ablation threshold depend on the wavelength of the laser?

2.4.1 Dependency of Ablation Threshold on the Number of Applied Pulses - Incubation

As predicted by the incubation model (equation 1.44):

$$F_{th}(N) = F_{th}(1) * N^{S-1}$$

which is described before in section (1.3.2), the ablation threshold decreases with the number of laser pulses applied to the same spot. This can already be seen for example in figure 2.10, as in the first row of ablation craters, the spot with 1 pulse is only barely visible and it gets bigger as the number of pulses increases.

If all of the fitted Liu-curves of one sample are plotted in the same graph, it gets even clearer, as the curves should be parallel to each other (ω_0 is constant), only the intersection with the X-axis decreases (ablation threshold energy). Such an exemplary plot can be seen in figure 2.16.

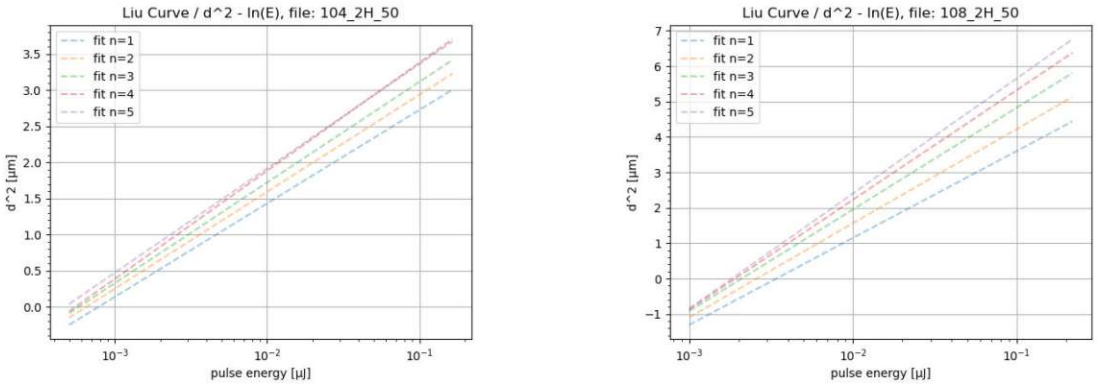

Figure 2.16: Plots of all of the fitted Liu-curves corresponding to the ablation threshold test of 25 *nm* CrN on sapphire (fig 2.10) on the left and the same coating and the same experiment, only with ceramic as a substrate, on the right.

If the logarithms of the threshold fluences are now plotted against the logarithm of the number of applied pulses, indeed a very linear trend of the data points can be seen (see figure 2.17), as suggested by the incubation model (equation 1.44): $F_{th}(N) = F_{th}(1) * N^{S-1}$.

Again, a least-squares curve can be fitted to the data points, which yields the incubation coefficient S (or ξ) proportional to the slope of this linear curve. If S=1, no incubation is present and the ablation threshold stays constant, even if the number of laser pulses per spot increases. If S<1, the smaller the incubation coefficient, the higher the incubation effect and therefore the faster the ablation threshold decreases with increasing pulse numbers.

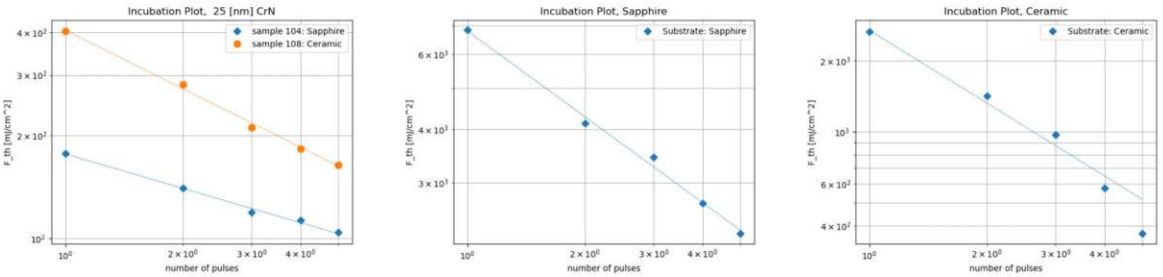

Figure 2.17: Incubation plots with the ablation threshold fluences determined from the ablation threshold experiments (Liu-curves) as markers and the fitted curve corresponding the incubation model as dashed line. On the left the graph of 25 *nm* CrN on sapphire and ceramic, in the middle the graph of a sapphire substrate alone, and on the right the graph of a ceramic substrate alone can be seen.

This phenomenon of decreasing ablation threshold with increasing pulse numbers could be advantageous in the case of an application of the results of this thesis as an optical data carrier, as less pulse energy would be required, which makes the engineering of the optical path easier and maybe also enables parallelization of the writing process.

On the other hand, for a possible application in optical data storage, a decrease in writing speed or an increase of the spot diameter could arise, if many pulses per spot would be used. A decrease in writing speed could arise, because the sample has to be stopped at a particular location for a period of time in order for the Laser to apply multiple pulses. An increasing spot diameter could be the result of consecutive pulses ending up at slightly different coordinates shifted relative to the first pulse of the pulse-train, if the laser is scanned over the surface of the sample.

2.4.2 Dependency of Ablation Threshold on the Coating Thickness

As it is already evident in the images of the experiments, that a higher energy level is necessary for ablation of thicker coatings, see figure 2.18, a closer look at the determined threshold fluences seems to be a logic step.

In figure 2.19 threshold fluence is plotted over the coating thickness, and it is clearly

evident, that with decreasing thin film thickness also the ablation threshold decreases. This behavior holds true for all of the samples tested in this thesis.

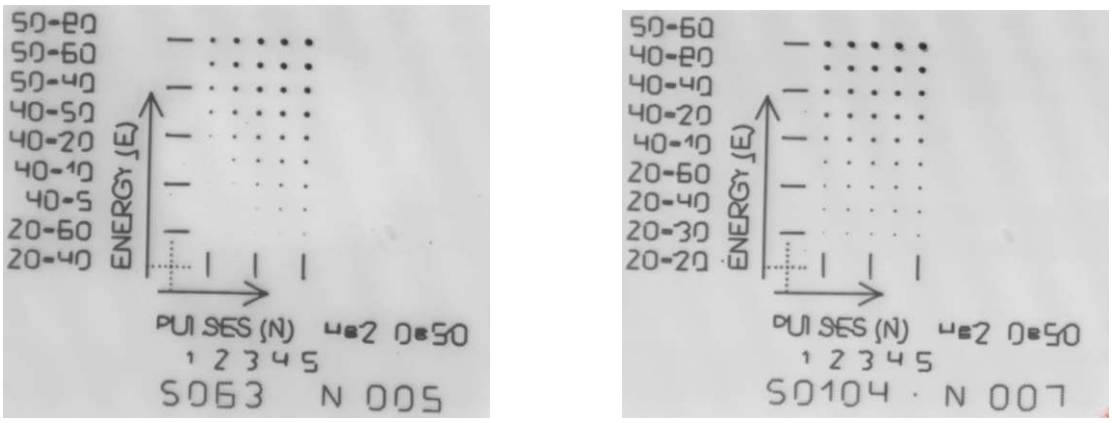

Figure 2.18: Images of the ablation threshold experiment of 100 *nm* CrN on a sapphire substrate on the left and 25 *nm* on the right. It is clearly evident, that in case of the thicker coating the fluence necessary for ablation has to be higher, since the energy level starts at a higher value and the first ablation spots are not even detectable.

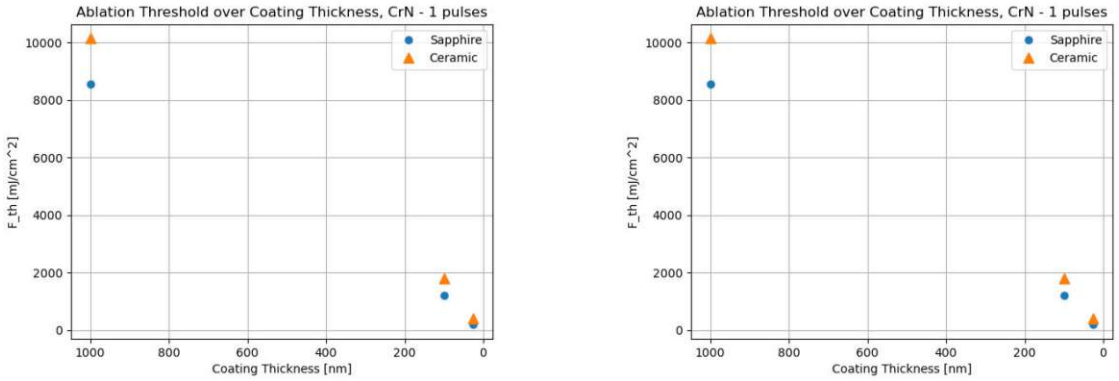

Figure 2.19: Ablation threshold plotted over the coating thickness for n=1 pulse on the left and n=5 pulses on the right. Values for both thin film systems of CrN with Sapphire and Ceramic as substrate can be found in each plot.

Again, in case of an application in data storage, first of all a smaller coating thickness could be beneficial because lower energy levels are required for the writing process. Second of all, thinner films allow smaller feature sizes, which will be elaborated in more detail in a following section.

2.4.3 Dependency of Ablation Threshold on the Substrate Material

In figure 2.19, beyond a decreasing threshold with decreasing film thickness, it is also visible, that the ablation threshold is higher for the ceramic substrate, even though the other parameters as coating material and thickness are the same. This phenomenon is again already visible in the images of the experiments, see figure 2.20, and is also true for all of the tested samples.

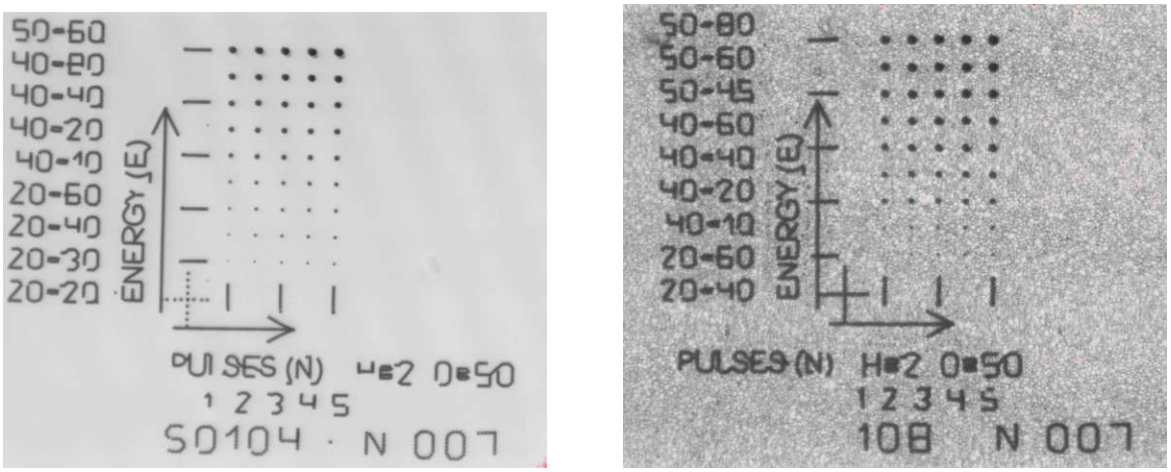

Figure 2.20: Images of the ablation threshold experiment of 25 *nm* CrN on a sapphire substrate on the left and a ceramic substrate on the right. It is clearly evident, that in case of the ceramic substrate the fluence necessary for ablation has to be higher, since the energy level starts at a higher value and the first ablation spot is not even detectable.

This behavior could be an indication, that the experimentally determined threshold values depend strongly on the properties of the interface between thin film and substrate. The higher values of the same coatings on ceramic could result from a better "adhesion" to this substrate.

Furthermore, in the image of the sample with the ceramic substrate a very granular surface can be seen. This presumably originates from the substrate manufacturing, which is probably some sort of sintering process, and the grains resulting from the sintered powder favor the formation of grains in the coating. This hypothesis is also supported by the fact, that there is no visible difference in the structure of uncoated and coated ceramic substrates.

Because of the higher ablation threshold and the seemingly bigger minimum ablation spots, sapphire seems to be the better suited substrate of choice for a potential application in optical data storage.

2.4.4 Dependency of Ablation Threshold on the Laser Wavelength

As the micro-machining workstation offers harmonics generation of the laser source, the ablation threshold was also determined at different wavelengths (see figure 2.21). The base wavelength is 1030 nm, therefore the 2^{nd} harmonic has a wavelength of 515 nm and the 3^{rd} harmonic 343 nm.

Figure 2.21: Images of the ablation threshold experiments of 25 nm CrN on sapphire with a laser wavelength of 1030 $nm = 1^{st}$ harmonic on the left, 515 $nm = 2^{nd}$ harmonic in the middle and 343 $nm = 3^{rd}$ harmonic on the right.

A direct comparison of the images of the experiment in figure 2.21 is not feasible, since the output Power of the Laser is dependent on the chosen harmonic and is only about 50% and 25% for the second and third harmonic respectively.

Also the beam diameter varies with the chosen laser harmonic, as the beam radius r is set to a different value for each wavelength by the supplier and the Gaussian beam radius w_0 depends on the wavelength. Therefore, the approximation of equation 2.4 was repeated with the measured beam diameters at the entrance pupil of the focusing objective, a plot of the experimentally determined beam diameters can be seen in figure 2.22:

$$1^{st} \text{ harmonic} = 1030\ nm \quad \dots \quad r = 1.25\ mm$$
$$w_{0,1030} \approx 1.1\ \mu m \tag{2.6}$$

$$2^{nd}\ harmonic = 515\ nm \quad \dots \quad r = 1\ mm$$
$$w_{0,515} \approx 0.68\ \mu m \tag{2.7}$$

$$3^{rd} \text{ harmonic} = 343\ nm \quad \dots \quad r = 1.3\ mm$$
$$w_{0,343} \approx 0.35\ \mu m \tag{2.8}$$

Figure 2.22 shows a good correlation to the approximated values above, which indicates a reasonable validity of the results of the conducted experiments. These results and

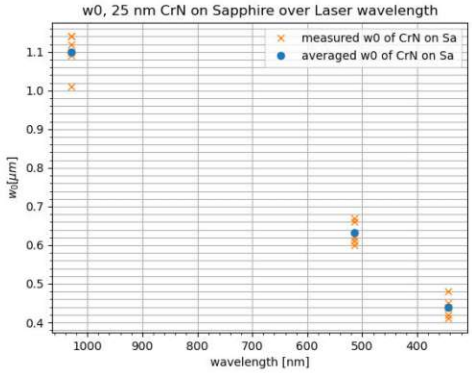

Figure 2.22: Plot of the experimentally determined Gaussian beam diameters w_0 of 25 nm CrN on a sapphire substrate over the used laser wavelength. The markers indicate the average, the error bars show the range of the maximum to the minimum measured value.

therefore the determined ablation threshold energies, as well as the ablation threshold fluences over the Laser wavelength are plotted in figure 2.23.

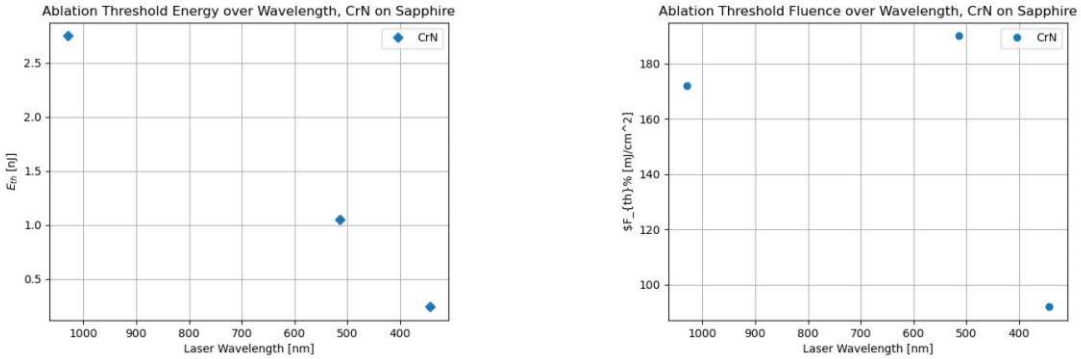

Figure 2.23: Plot of the ablation threshold energy (left) and fluence (right) over the Laser wavelength corresponding to the experiments depicted in figure 2.21.

In figure 2.23 it is apparent, that the threshold energy decreases with decreasing laser wavelength, but since the beam diameter and therefore also ω_0 varies between the harmonics, the threshold fluences do not follow this trend. However, at the NUV wavelength the threshold fluence is substantially lower compared to the NIR and VIS wavelengths.

Furthermore, as it can be seen in figure 2.21, with decreasing Laser wavelength also the possible feature size decreases, which correlates very well with the approximation in equation 2.4 or the very well known *Abbe-Limit*:

$$d_{Abbe} = \frac{\lambda}{2 * NA} \tag{2.9}$$

Both the lower threshold and the smaller feature size favor the NUV wavelength of 343 nm in terms of an application in data storage, the limit for the smallest possible feature size will be discussed in the following section.

2.5 Determination of minimum Ablation Spots

Because of the non-linear nature of the ablation mechanism and the above mentioned decrease in feature size with decreasing wavelength, the question of finding the limit of this process arises.

Moreover, from a possible data storage application perspective, the data density on a given surface area is inversely proportional to the square of the diameter of one ablation spot, which equals one Bit of data. In other words, if the feature size decreases by $\frac{1}{2}$, there is space for 4 times as many spots on the same surface area, than with the original feature size.

In order to find the feature size limit the 3^{rd} harmonic of the Laser at 343 nm, CrN as a coating and a thickness of 10 nm was chosen, where a test pattern was ablated with varying feature sizes and laser energies.

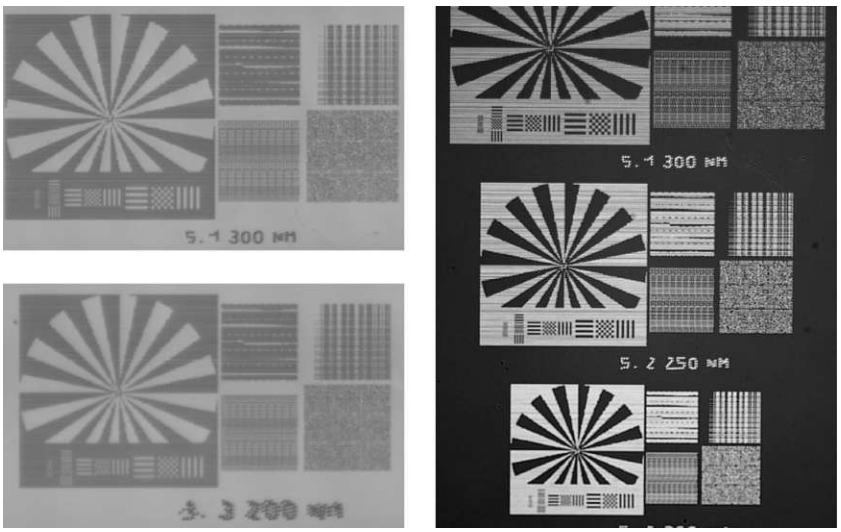

Figure 2.24: Images of the parameter test in order to experimentally determine the smallest possible feature size of the ablation process. Experiments were done on 10 nm CrN on a glass substrate with 343 nm laser wavelength.

The images in 2.24 were taken with trans- (right) and epi-illumination (left), and it is apparent, that features down to about 250 nm can barely be separated. This is well below the used wavelength of 343 nm and also below the Abbe-limit, and can be explained by the non-linear ablation mechanism, where the resulting ablated spot can be smaller than the Gauss-radius w_0 (see also figure 1.9). It is also worth mentioning, that some of the structures are so small, that they cannot be examined reasonably well with the method available in this thesis and other techniques with higher resolution should be considered.

Because of the very small ablation spot, the determination of the minimum feature size does not seem to be limited by the ablation, but rather by the evaluation process, which currently is microscopy. The features resulting from the ablation process can be

smaller than, but the resolution of an optical microscope is limited by the Abbe-limit (equation 2.9):

$$d_{Abbe} = \frac{\lambda}{2 * NA}$$

In order to increase the resolution of the evaluation system the illuminating wavelength of the microscope could be reduced, which is also limited, or another method like Scanning-Electron-Microscopy (SEM) could be utilized. In the case of a possible data storage application, SEM would probably not be practical, as image generation per-se is slower and also sample preparation is more difficult than with optical microscopes (measurement in vacuum).

All in all, the experiments to determine the smallest feature size possible by the single-beam ablation process used in this thesis yielded the very interesting finding, that no quantitative measure can be determined, since the features are too small to be resolved by the available techniques. Implications of these promising results for a possible application in data storage will be discussed in the following section.

3 Discussion of the Results

In this thesis different samples, coated via PVD, with various coating and substrate materials have been examined in terms of ablation threshold. The mathematical model of the non-linear ablation process of Liu (see equation 1.36 in section 1.3.1) seems to be feasible and has been used to experimentally determine the ablation thresholds.

It has been found, that there are several influences on this threshold, which are listed below:

- number of pulses applied to one spot: with an increasing number of pulses the ablation threshold decreases (Incubation)
- coating thickness: smaller thicknesses yield lower ablation thresholds
- coating material: different coating materials have different ablation thresholds - CrN and AlCrN seem to have the lowest ones (out of the samples in this thesis)
- substrate: the ablation thresholds of the samples with sapphire as a substrate have lower ablation thresholds than the ones on ceramic - the interaction zone possibly dictates ablation behavior
- laser wavelength: the 1^{st} and 2^{nd} harmonic (1030 and 515 nm) yielded comparable ablation thresholds, the one for the 3^{rd} (343 nm) seems to be substantially lower for the materials tested in this thesis

As mentioned before, only one experiment was carried out on each combination of substrate (sapphire, ceramic) plus coating (Cr, CrN, Cr_2O_3, CrB_2, $AlCrN$) and the thickness steps (1000, 100, 25 nm), so because of that and because of the uncertainty in the focal beam diameter more experiments have to be carried out and a better way of focal beam diameter determination should be found in order to get statistically more reliable data.

However, the goal of this thesis was to compare the available samples to each other and find trends, in order to determine the feasibility of a thin film system as an optical data carrier.

Referring to the above mentioned findings and because of the following reasons specific for this application, 10 nm CrN or AlCrN on a glass substrate seem to be the coating, thickness and substrate of choice with the highest potential for a successful application as an optical data carrier:

- lowest ablation threshold (of the tested coatings)

- smallest ablation diameters possible (thin coating + short wavelength)
- high contrast between ablated spots and unprocessed coating (high signal to noise ratio)
- possibly highest durability (Cr alone is possibly prone to oxidation, CrN is probably more durable)
- lowest cost (thin glass + PVD coating already in mass production, e.g. smartphone screens)

3.1 Possibilities, Limitations and Perspective

3.1.1 Application Possibilities

The technique of ablating a thin coating on some sort of substrate, possibly glass as discussed above, in order to "write" dots/spots/pixel/bit and therefore store data turned out to be feasible and opens the possibility to use it as a form of optical data storage. Also the "reading" process does not seem to be a difficult issue as long as the feature size is big enough, as the written patterns can be seen with any standard microscope, trans- and epi-illumination have been shown in this thesis.

Furthermore, as this technique is not limited by the desired pattern of the ablated spots, any existing or possibly new data format, which can be read optically, could be used, for example simple text, analog black and white images, digital codes as QR-Codes, or even hybrid forms, see figures 3.1, 3.2, 3.3.

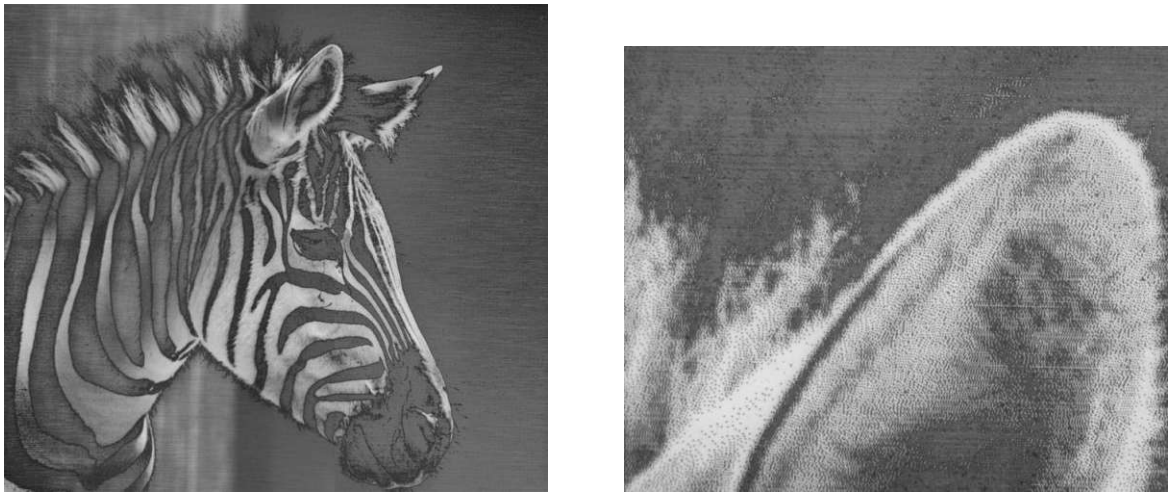

Figure 3.1: Microscope images with 10x (left) and 50x (right) magnification of an analog image of a Zebra ablated with 1 μm pixel size on a sample with 10 nm CrN and a glass substrate.

In figure 3.1 a grey-scale image of a Zebra has been dithered and written on a sample of 10 nm CrN on glass with a pixel-size of 1 μm, which would be beneficial, for example, if

data has to be passed between different parties where no decoding is desired so the data can be seen directly.

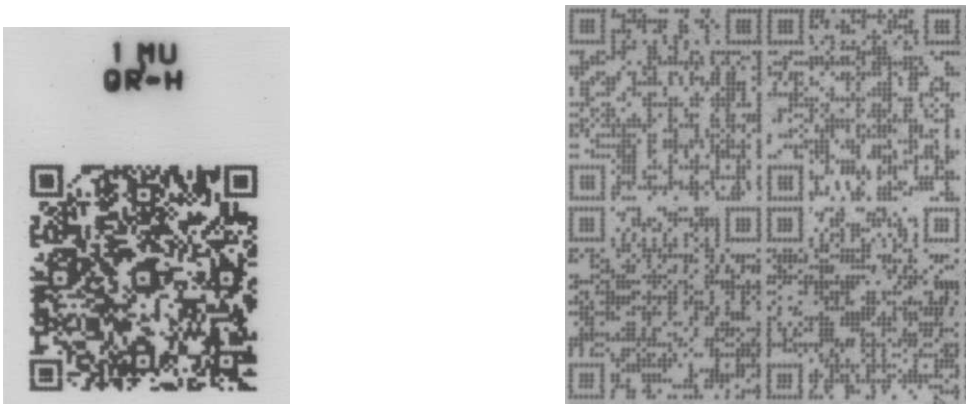

Figure 3.2: Microscope images with 100x magnification of a single QR-Code on the left and a matrix of QR-Codes on the right, ablated with 1 μm pixel size on a sample with 10 nm CrN on a glass substrate.

In contrast to the analog format in figure 3.1, in figure 3.2 a digital format in the form of a QR-Code is shown, which would be advantageous if abstract data has to be stored and an efficient use of the available area is desired, as these Codes can vary in size and can be arranged in a matrix (see fig. 3.2 on the right).

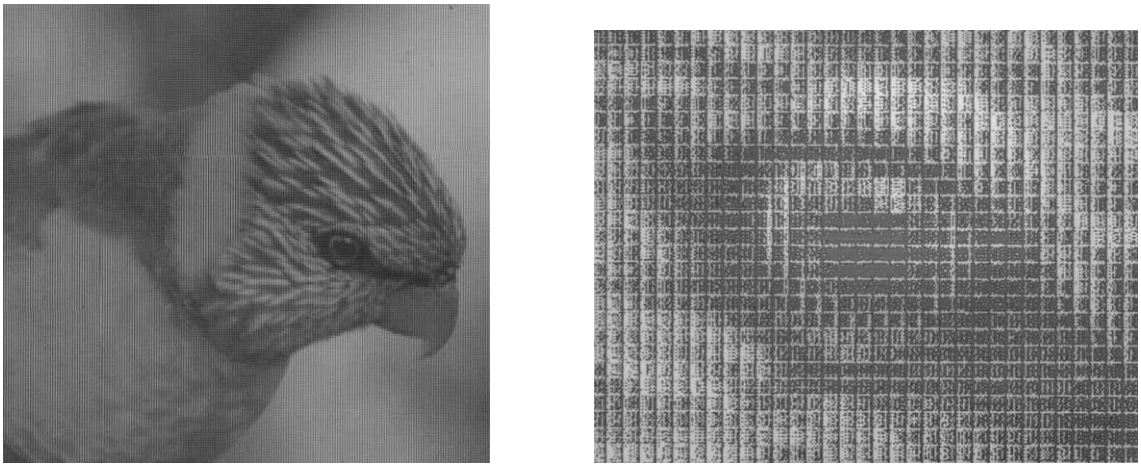

Figure 3.3: Microscope images with 10x (left) and 50x (right) magnification of a hybrid analogue/digital image of a parrot ablated with 1 μm pixel size on a sample with 10 nm CrN on a glass substrate.

In figure 3.3 a hybrid form of analog and digital storage of an image of a parrot is shown, where the image as a whole can be interpreted as a grey-scale one, but each grey-scale pixel digitally contains color information in form of 255-bit RGB values (3 sub-pixel columns).

3.1.2 Limitations

As described above, the technique of ablating spots on a thin film sample in order to optically store data is not limited by the format of this data and can be utilized in different ways. However, the application as optical data storage is limited in terms of data density (size of ablation spots) and "writing" speed. The pixel size can only be as small, as the "reading" system is capable of resolving and since in this thesis an XYZ-stage was used the speed is limited by the mechanical properties of it. In order to put it in perspective, the data density and the writing speed will be approximated.

If an area of 100 cm^2 is assumed (approximately the writeable area of a CD / DVD / Blu-ray), one data carrier could store the following maximum amount of raw data, depending on the size of one bit (= one laser ablated spot):

$$\text{data capacity in } byte = \frac{\text{writeable area}}{\text{diameter of ablated spots}^2 * 8}$$

with 1 $byte = 8$ bit, and the diameter of ablated spots d (= 1 bit)

$$d = 1\ \mu m \quad \ldots \quad 1.25\ GB \tag{3.1}$$

$$d = 0.5\ \mu m \quad \ldots \quad 5\ GB \tag{3.2}$$

$$d = 0.3\ \mu m \quad \ldots \quad 13.9\ GB \tag{3.3}$$

The "writing speed" of raw data, for the single-beam ablation process aforementioned, can be extrapolated for different average velocities of the stage to the following values:

$$\text{writing speed } \frac{byte}{s} = \frac{\text{average stage velocity } v_{\text{avg}}}{\text{diameter of ablated spots } d * 8}$$

with $8\ \frac{bit}{byte}$, and $d = 0.5\ \mu m$

$$v_{\text{avg}} = 200\frac{mm}{s} \quad \ldots \quad 0.05\ \frac{MB}{s} \tag{3.4}$$

$$v_{\text{avg}} = 500\frac{mm}{s} \quad \ldots \quad 0.125\ \frac{MB}{s} \tag{3.5}$$

$$v_{\text{avg}} = 1000\frac{mm}{s} \quad \ldots \quad 0.25\ \frac{MB}{s} \tag{3.6}$$

3.1.3 Summary and Perspective

It has been shown, that it is feasible to write data in the form of ablation spots on a system consisting of a substrate with a thin film coating. CrN with a very small thickness of 10 nm yielded the most promising results and will be examined in more detail in upcoming experiments. Also, the possible pixel size turned out to be smaller than expected, resulting in diameters of the ablated spots which are smaller than the resolution limit of the built-in microscope.

However, the method of evaluating the ablation threshold is labor-intensive and therefore slow and furthermore it is prone to errors and not accurate enough. Because of these factors further experiments have to be done to first of all determine at least the Gaussian beam radius w_0 with a high accuracy and independent of the ablation threshold, and second to automate parts of the experiments in order to conduct a higher number of measurements and therefore get statistically viable results with error margins that can be estimated.

All in all, the scope of this thesis has been examined successfully and yielded very interesting and promising results, both in terms of the questions posed at the beginning of this work, as well as new phenomena and ideas that have emerged during the experiments and the evaluation of the results, as the possibly strong dependency of the ablation threshold on the transition zone between coating and substrate. This thesis does not mark the end, but rather the initiation of research in the field of long-term data storage and exciting experiments and developments are expected to happen.

Acronyms

List of Acronyms

- **AOI** Angle of Incidence
- **CNC** Computer Numerical Control
- **CVD** Chemical Vapor Deposition
- **DLIP** Direct Laser Interference Patterning
- **DOE** Diffractive Optical Element
- **DOF** Degree of Freedom
- **GVD** Group Velocity Dispersion
- **HAZ** Heat Affected Zone
- **KLM** Kerr Lens Mode-Locking
- **LASER** Light Amplification by Stimulated Emission of Radiation
- **PVD** Physical Vapor Deposition
- **SAM** Self Amplitude Modulation
- **SPM** Self Phase Modulation

List of Figures

References

[1] Chandra S. R. Nathala et al. “Ultrashort laser pulse ablation of copper, silicon and gelatin: effect of the pulse duration on the ablation thresholds and the incubation coefficients”. In: *Applied Physics A, Materials Science and Processing* (2016).

[2] Mustafa H. et al. “Picosecond-pulsed laser ablation of zinc: crater morphology and comparison of methods to determine ablation threshold”. In: *Optics Express* 18664 (2018).

[3] Zhanliang Sun et al. “Generic Incubation Law for Laser Damage and Ablation Thresholds”. In: *Applied Physics* 117 (7) (2015).

[4] Klemens Jesse. *Femtosekundenlaser, Einführung in die Technologie der ultrakurzen Lichtimpulse*. Springer Vierweg, 2016. ISBN: 978-3-662-49356-4.

[5] Liu J. M. “Simple technique for measurments of pulsed Gaussian-beam spot sizes”. In: *Optics Letters* Vol. 7, No. 5 (1982).

[6] Donald M. Mattox. *Handbook of Physical Vapor Deposition (PVD) Processing*. ELSEVIER, 2010. ISBN: 978-0-8155-2037-5.

[7] Paul Heinz Mayrhofer. *Lecture Surface Technology*. E308 Institute of Materials Science and Technology, TU Vienna, 2021.

[8] Donald Strickland and Gerard Mourou. “Compression of Amplified Chirped Optical Pulses”. In: *Optics Communications* (1985).

[9] Andrew M. Weiner. *Ultrafast Optics*. John Wiley and Sons, Inc., 2009. ISBN: 978-0-471-41539-8.